A Portable and Convenient System for Unknown Liquid Identification With Smartphone Vibration

Yongzhi Huang, *Student Member, IEEE*, Kaixin Chen, Yandao Huang, Lu Wang, *Senior Member, IEEE*, and Kaishun Wu, *Senior Member, IEEE*

Abstract—Traditional liquid identification instruments are often unavailable to the general public. This paper shows the feasibility of identifying unknown liquids with commercial lightweight devices, such as a smartphone. The wisdom arises from the fact that different liquid molecules have various viscosity coefficients, so they need to overcome dissimilitude energy barriers during relative motion. With this intuition in mind, we introduce a novel model that measures liquids' viscosity based on active vibration. The idea sounds straightforward, yet, it is challenging to build up a robust system utilizing the built-in accelerometer in smartphones. Practical issues include under-sampling, self-interference, and volume change impact. Instead of using machine learning techniques, we tackle these issues through multiple signal processing stages to reconstruct the original signals and cancel out the interference. Our approach achieved the liquid viscosity estimates with a mean relative error of 2.3% and distinguish 30 kinds of liquid with an average accuracy of 97.33%.

Index Terms—Liquid, viscosity coefficient, identification, mobile sensing, ubiquitous computing

1 Introduction

Motivation. Liquid testing has recently attracted significant interest. Researches have led to solutions that deliver inexpensive and ubiquitous liquid testing outside the lab environment[1], [2], [3], [4], [5]. The potential application scenarios of ubiquitous liquid testing range from safety inspection in public transportation, identification of fake luxury perfume, detection of water contamination in countries with limited sanitary water facilities, monitoring daily nutrition intake from drinks, in-home urine testing to track disease progression, etc.

Unfortunately, the proposed liquid testing systems require specialized external devices like RFID readers [1], [2], photodiodes [3], ultra-wideband (UWB) units [4], and piezoelectric sensors [5]. The difficulty in deploying and using for the general public prevents those systems from penetrating our daily life. CapCam [6] is the first and only work that measures liquids' surface tension only with a smartphone. However, it requires prior knowledge about the transparent liquid (such as measuring the density of liquids in advance), and thus it is unable to identify unknown liquids.

In this paper, we try to ask whether we can identify unknown liquids (the liquid in the container without information leaking out) with a commercial device, such as a smartphone. To answer this question, we need to find a novel property, and it is unique to different liquids and accessible to smartphones. Fortunately, we found viscosity, an inherent property of liquid. Viscosity describes the resistance force generated by the relative movement of liquid molecules. Different liquid molecules have various viscosity coefficients, so they need to overcome different energy barriers during relative motion. If we can measure the liquid viscosity, we can identify the liquid type and analyze the liquid concentration. However, conventional viscosity testing instruments [7], [8], [9], [10], [11], [12] are expensive and invasive. It will also contaminate the liquid when measuring the viscosity with a rotatable probe. How to measure the liquid viscosity with a smartphone remains unknown.

Our Approach. In this paper, we present Vi-Liquid,[1] a lightweight smartphone application that measures the liquid viscosity for unknown liquid testing by leveraging only a built-in vibro-motor and an accelerometer. As shown in Fig. 1, to measure the liquid viscosity, the user attaches the smartphone to the container and activates the app. Afterwards, Vi-Liquid generates active vibration signals through the built-in vibro-motor and collects the reflected vibration signals using a built-in accelerometer. The signals are feed into our proposed Vibration-Viscosity model to calculate the viscosity result. The critical insight behind Vi-Liquid is that the liquid will creates a viscosity-related resistance force when giving an

- *Yongzhi Huang, Kaixin Chen, Yandao Huang, and Lu Wang are with the College of Computer Science and Software Engineering, Shenzhen University, Shenzhen 518060, China. E-mail: {huangyongzhi, 2017133035, 2016040084}@email.szu.edu.cn, wanglu@szu.edu.cn.*
- *Kaishun Wu is with the College of Computer Science and Software Engineering, Shenzhen University, Shenzhen 518060, China, and with the PCL Research Center of Networks and Communications, Peng Cheng Laboratory, Shenzhen 518066, China, and also with the Guangzhou HKUST Fok Ying Tung Research Institute, Guangzhou 511458, China. E-mail: wu@szu.edu.cn.*

Manuscript received 16 Mar. 2021; revised 12 July 2021; accepted 16 Sept. 2021. Date of publication 20 Oct. 2021; date of current version 6 Mar. 2023.
This work was supported in part by the China NSFC under Grants U2001207, 61872248, and 61872246, in part by the Guangdong NSF under Grant 2017A030312008, in part by the Shenzhen Science and Technology Foundation under Grants ZDSYS20190902092853047 and R2020A045, in part by the Project of DEGP under Grants 2019KCXTD005 and 2021ZDZX1068, in part by the Guangdong "Pearl River Talent Recruitment Program" under Grant 2019ZT08X603, in part by the Guangdong Science and Technology Foundation under Grants 2019B111103001 and 2019B020209001, Guangdong Special Support Program.
(Corresponding author: Lu Wang.)
Digital Object Identifier no. 10.1109/TMC.2021.3121332

1. https://youtu.be/Gpt5eJXHFBQ

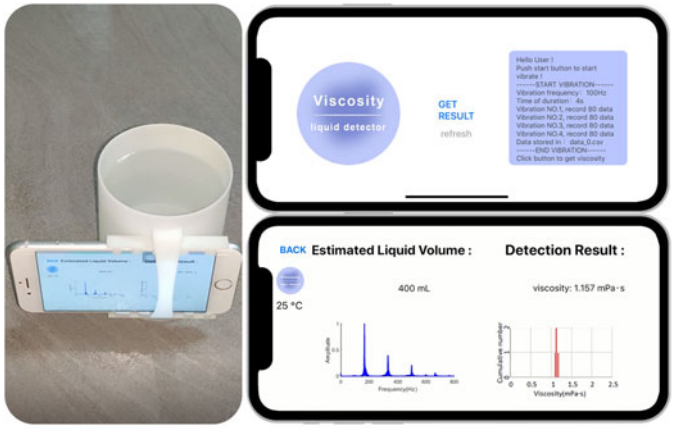

Fig. 1. (a) Using iPhone 7 to detect unknown liquid. (b) The user interface.

external activation, as the active vibration from a vibro-motor. We can calculate the viscosity by analyzing the received vibration signal affected by this resistance force.

Challenges and Solutions. However, it is non-trivial to measure the liquid viscosity using active vibration signals generated from a smartphone. To ensure accuracy, reliability, and usability, we have to address three challenges: (i) First, it is unclear how to calculate the viscosity by leveraging the influence and physical characters from active vibration to the liquid. It is necessary to build up a model that represents the relationship between vibration signals and liquid viscosity. (ii) Second, the intrinsic restriction of hardware settings regarding vibro-motor and accelerometer in smartphones poses another challenge to the vibration signal's design and analysis. As the maximum sampling rate through API is limited to 100 Hz in the COTS smartphones, the sampled signals are distorted and causing considerable measurement errors. (iii) Third, in practical usage, we encounter two main interferences. One comes from the self-interference. When the vibration signal transmits directly to the accelerometer, it overwhelms the low SNR signal reflected from the target liquid. The other is that the change of liquid volume results in different signal patterns, making the viscosity measurement inconsistent even if they are the same liquid.

To address the first challenge, we build the kinematics equation of single-degree-of-freedom to link the liquid viscosity, the *shearing force* from liquid to the container, and the vibration signal together. We observe that the amplitude of the reflected vibration signal in *steady-state* is affected by the *shearing force*, and the attenuation in *decaying-state* is dominant by the viscosity-related damping coefficient. Then we verify the proposed model with several experiments in the feasibility study. The second challenge is to solve the system safety mechanism on sampling restriction. We need to restore the undersampled signal, termed *Supersampling Rate Reconstruction*. This algorithm utilizes the phase shift of the vibration signal to combine the sample points of multiple periods into one period. We further improve the restored signal by applying *orthogonal matching pursuit* to recover the complete signal and enhanced the processing efficiency. To deal with the third challenge, we subtract the pre-recorded straight path signals from the received vibration signals to cancel the straight interference. In the next stage, we set a series of weights for each liquid volume to calibrate the amplitude affected by the liquid's volume change.

Summary of Experiment Results. Vi-Liquid has high accuracy for viscosity measurement, and the mean relative error for 30 kinds of liquids is only 2.3%. Within this error range, Vi-Liquid can also identify liquids with an average accuracy of 96.26%, including highly similar beverages, such as Coca-Cola and Pepsi. It can also accurately distinguish liquids based on the content of different mass concentrations of salt, sugar, and fat. Distinguish pollution water has only 2.33% mean relative error. Furthermore, Vi-Liquid identifies uric acid and urine protein in urine with errors of 1.13 mg/100 mL and 0.18 mg/100 mL, respectively. The urine test function with this error range can be used as *at-home diagnostic monitor* and *health admonishes* to identify common asymptomatic diseases, such as nephritis, with the uric acid concentration higher than 60 mg/100 mL [13] and protein concentration higher than 3 mg/100 mL complication [14]. Our error inidentifying alcohol concentration is only 1.38% by mass, which can well allow users to avoid the health risks caused by alcohol.

Contributions. The main contributions in Vi-Liquid summarise as follows:

- We propose Vi-Liquid to identify unknown liquid based on viscosity using smartphone-generated vibration, which is the first work that identifies unknown liquid only with a smartphone to the best of our knowledge. Vi-Liquid can detect water contamination, monitor alcohol intake, and measure uric acid and protein concentration in urine.
- We establish a viscosity measurement model using vibration signals and verify its feasibility. We propose multiple stages of approaches to overcome several practical issues and build up a robust system.
- We implement Vi-Liquid as an efficient application running on a COTS iOS smartphone and validate its performance through comprehensive experiments. On average, our system yields a viscosity estimation error of 2.3% compared to that of 1% obtained by the high-cost viscosity instrument.

The rest of the paper is organized as follows: In Section 2, we detail why vibro-motor and accelerometer modules can indicate the feature of liquid viscosity from theoretical models. We give the feasibility study by analyzing the received vibration readings in Section 3. After the system overview in Section 4, we introduce the system design and illustrate how we address the challenges when migrating the system to a smartphone in Section 5. In Section 6, we present several case studies to evaluate our system performance on a smartphone. We discuss the related work in Section 7. Finally, we give the conclusion and future work in Section 8.

2 Vibration Model for Viscosity Measurement

In this section, we will introduce the theoretical models for liquid detection.

2.1 Liquid Viscosity and the Shearing Force

Viscosity is an essential physical attribute of liquids. When liquid molecules move in space, they have to overcome the

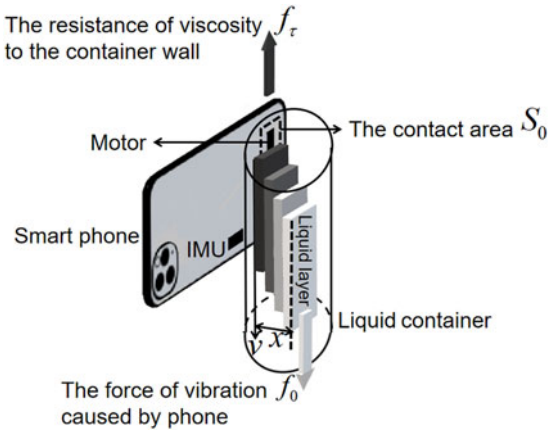

Fig. 2. The detection model of Vi-Liquid.

friction caused by the relative motion between them, which accounts for liquid molecules' viscosity in the microscopic [15], [16]. The higher the force between molecules, the more significant the energy barrier. The viscosity η can be expressed as

$$\eta = \frac{hN}{V}\mathbf{e}^{-\frac{\Delta G}{RTemperature}}, \tag{1}$$

where V is the molar volume of the molecule, ΔG is the Gibbs energy change of the molecule, $Temperature$ is the temperature, h, N and R are Prang Gram constant, Avogadro constant, and Boltzmann constant, respectively. We assume the indoor temperature is stable and regard $Temperature$ as a constant. Different kinds of the molecule have diverse Gibbs energy, which indicates the energy-consuming for each molecule's unit distance movement. The Gibbs energy change and molar volume of the molecule are various for each kind of molecule. Therefore, the liquids can be distinguished by their viscosity. For instance, the viscosity of distilled water, ethyl alcohol, and honey are 1 cP, 1.2 cP, and 3000 cP[2] at 20 °C .

In macroscopic observations [17], a liquid's viscosity characterizes the frictional force between different liquid layers, as shown in Fig. 2. Given an external force f_0, the resistance force between liquid and container is a shearing force f_τ that can be modeled as follows:

$$f_\tau = \eta S_0 \frac{v}{x}, \tag{2}$$

where S_0 is the contact area between the liquid layer and container, and v is the movement speed of the liquid. x refers to the layer depth of moving liquid. Given a certain liquid volume and vibration, the S_0, v, and x can be considered as constants. Thus, we can measure the viscosity η by leveraging its linear relationship with f_τ.

2.2 Viscosity Calculation Leveraging Vibration

However, it is still non-trivial to measure the viscosity using a smartphone with the theory discussed above. In this section, we illustrate the viscosity calculation model using a smartphone. During the measurement, the built-in vibro-motor generates vibration actively outside the liquid container. Due to the characteristic of liquid viscosity, a resistance force (i.e., the shearing force) will occur when the liquid flow. Our purpose is to detect this shearing force using the accelerometer, and what's more, to calculate the viscosity.

Specifically, we can separate the vibration into three states: the transient, the steady, and the decaying-state. We eliminate the vibration signals in transient-state, which last a short time in the beginning since it is highly dynamic and intractable to model. When it comes to steady-state, we consider the vibrated liquid layer as a study object and model a spring-mass-damper model of single-degree-of-freedom. Given the constant external force f_0 caused by the motor as a sinusoidal vibration, we have

$$m\frac{\mathrm{d}^2x(t)}{\mathrm{d}t^2} + \beta\frac{\mathrm{d}x(t)}{\mathrm{d}t} + kx(t) = (f_0 - f_\tau)\sin(\omega t). \tag{3}$$

Among them, m is the mass of the vibrated liquid layer (known as the Stokes boundary layer [14]). β is a damping coefficient affected by viscosity. The elastic coefficient k is mainly affected by the container, and it is a constant that we can obtain by looking up the datasheet [18]. ω is the angular frequency of the vibro-motor. The particular solution of the Differential Equation (3) is

$$x_{vib}(t) = \frac{f_0 - f_\tau}{\sqrt{(k-\omega^2 m)^2 + (\beta\omega)^2}}\sin(\omega t - \phi), \tag{4}$$

where $\phi = \arctan(\frac{\beta\omega}{k-m\omega^2})$. Owing to the frequency and intensity of the smartphone driving signal is constant, ω and f_0 are regarded as constant. Hence, we can estimate the viscosity from the maximum amplitude of the vibration A, without tracking the vibration trajectory.

$$A = \frac{f_0 - f_\tau}{\sqrt{(k-\omega^2 m)^2 + (\beta\omega)^2}}. \tag{5}$$

Next, we focus on the viscosity-related damping coefficient β. When the external force induced by the motor pause, the system turns to decaying-state, where the vibration of liquid gradually decays and then stops. The equation of motion in decaying-state is

$$m\frac{\mathrm{d}^2x(t)}{\mathrm{d}t^2} + \beta\frac{\mathrm{d}x(t)}{\mathrm{d}t} + kx(t) = 0, \tag{6}$$

where the general solution to the equation is

$$x_{decay}(t) = A\mathbf{e}^{-\frac{\beta}{2m}t}\sin\left(\sqrt{\frac{k}{m}}\sqrt{1-\left(\frac{\beta}{2\sqrt{km}}\right)^2}t + \theta\right). \tag{7}$$

As the amplitude attenuating constantly, we can record the amplitude of A_i in the same period T, and calculate the decaying factor Λ as

$$\Lambda = \frac{x_{decay}(t)}{x_{decay}(t+T)} = \mathbf{e}^{T\cdot\frac{\beta}{2m}}. \tag{8}$$

Therefore, we can use the attenuation of the amplitude in adjacent periods to assess the β. Note that the m is a constant that can calibrate in advanced. Specifically, when the motor is paused, we apply the peak amplitude values in

2. **cP** is a unit of viscosity, which can be also written as **mPa · s**

Fig. 3. Confirmatory experiments were set up by separate motor, accelerometer, container and alternating current power supply.

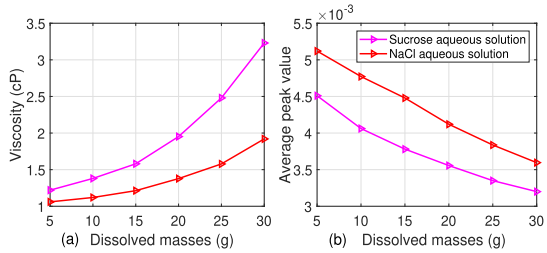

Fig. 4. Dissolving different mass of sucrose and NaCl in solution. (a) Change of viscosity. (b) Change of average peak value.

adjacent periods to calculate the decaying factor Λ and eliminate noise by averaging the results.

Next, we can calculate the resistance of f_τ leveraging the transient-state amplitude A. Finally, we can estimate the viscosity η based on the shearing force f_τ from the target liquid.

3 Feasibility Study

This section will verify the proposed model and demonstrate the feasibility of applying the standalone vibro-motor and accelerometer to measure liquid viscosity.

3.1 Experimental Setup

We utilized a 3D printer (Form 3) to print a 500 mL of tableware resin cup with two side slots at the position of 250 mL metric value. The vibro-motor (iPhone 7 Taptic Engine) and 3-axis accelerometer (BMI160) were deployed inside the slots, as shown in Fig. 3. We set the vibration frequency as 167 Hz, which is in line with the vibration frequency in the mobile phone we used (i.e., iPhone 7). In the data collection part, we set the accelerometer's sampling rate as 1600 Hz for high data resolution. We measured the viscosity through the shearing force, so only X-axis data are used for analysis. For the ground truth, we utilized a rotatory viscometer $ATAGO-VISCO^{TM}$ 895 to measure the liquid viscosity. It provides a measurement range from 1 to 3.5 $\times 10^8$ **cP** with a resolution of 0.01 **cP**. The ground truth measurement has a relative error of 1%. We run all the experiments in a laboratory with a stable room temperature at 25°C. Unless otherwise specified, the following experiments are conducted under the setting discussed above.

3.2 The Viscosity Uniqueness of Liquids

We first explore how different viscosity coefficients affect the vibration signals we received.

To control the influence of the two variables: mass and volume, making the liquid viscosity the only variable, we need to find two suitable liquids. The liquids should meet the condition that the volume growth rate is the same, but the viscosity growth rate is different when adding the same mass of the solutes. For instance, when we added dissimilitude solutes with the equivalent mass into the containers filling them with the same volume water, both liquids have the same volume increase, but diverse viscosity increases.

In our pilot study, we iterated the setting and found that, at 18°C, the sucrose aqueous solution and the NaCl aqueous solution meet the experimental conditions.

We constantly dissolved sucrose and NaCl to 450 mL of water and recorded their viscosity and vibration readings. From the results plotted in Fig. 4, we had following findings: From Fig. 4a, we could see that the higher the liquid concentration is, the higher the liquid viscosity we have; two liquids of the same volume and mass have distinctive viscosity coefficients. We noticed that, in Fig. 4b, the average peak value varies considerably even though the smallest viscosity gap is only 0.16 cP when the dissolved mass is 5 g, which interpret the viscosity will cause significant attenuation to the vibration. However, based on the results in Fig. 4b, the average peak value is related to both viscosity and mass of liquid. We still can not conclude that the peak value reveals the unique viscosity of the liquid. Therefore, we will further verify the findings in the next experiment.

3.3 The Impact of Mass

Can the mass affect the vibration signal? According to the model above, the liquid's mass is not an effect variable as it is the Stokes boundary layer mass, which is a constant. Accordingly, we will prove that the liquid's mass is independent in the following experiments. We prepared six liquids of different viscosity (10% and 20% sucrose solutions, whole milk, vinegar, soy sauce, and sugar-free coffee) in four volumes ($6 \times 4 = 24$ liquid samples in total). We recorded the average peak values of these samples' amplitude and mass and the results is demonstrated in Fig. 5.

We found that the mass variation does not correlate to the amplitude variation. Taking the green line (300 mL) as an example, we could observe that the whole milk with more mass results in a smaller amplitude than sucrose solution. It seems to be counter-intuitive. In fact, in fluid mechanics, this principle is called the Stokes boundary layer theory. We attached the sensor to the container's wall instead of the bottom, which was not disturbed by mass. According to the Stokes boundary theory, the container wall's vibration amplitude is tiny, so the affected liquid only a thin layer near the boundary. Compared with the density, the liquid is more affected by the surface area. Therefore, the variable mass refers to the liquid layer, and we can regard it as a constant.

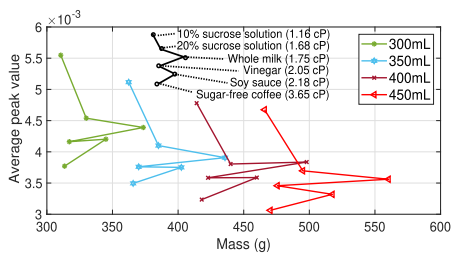

Fig. 5. The distribution of different volumes of liquid in the mass-amplitude graph.

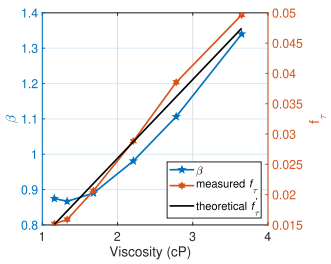

Fig. 6. The measured value β, f_τ and the theoretical f'_τ.

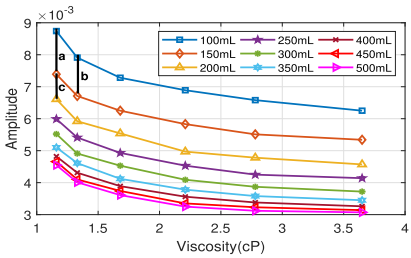

Fig. 7. The attenuation of volume to viscosity is not proportional.

3.4 The Volume Interference

On the other hand, the volume change has a more significant influence on the amplitude for the same liquids. Because the increase in liquid volume results in a larger contact area S_0. According to Equations (2) and (5), we have a larger shearing force f_τ, which leads to a smaller amplitude A. We detail the design of a calibration scheme for tackling this impact in Section 5.

The change of volume will also cause disturbance to vibration.

We use the viscometer to measure six groups of sucrose solutions with mass concentrations of 10%, 15%, 20%, 25%, 30%, and 35%. Their viscosity are 1.16 cP, 1.33 cP, 1.68 cP, 2.21 cP, 2.78 cP, and 3.65 cP, respectively. In order to verify the volume interference, we filled the container with different volumes of the sucrose solutions, then detected changes in amplitude from 100 mL to 500 mL. We measured fifty sets of data every 50 mL and calculated the average peak value of the amplitude. Through measurement, we found that although the volume has a negative correlation with the amplitude, the change interval is not proportional. As shown in Fig. 7, when the volume increases, the decay rate of amplitude gradually decreases (a $>$ c), and the decay is the same (a = b) although the viscosity is different.

3.5 Attenuation in Decaying-State

In this section, we explore the attenuation characteristic in liquids of the same volume but different viscosity in the decaying-state. We used a high sampling accelerometer to collect data. We filled with 400 mL sucrose solution in different concentrations (10%, 15%, 20%, 25%, 30%, and 35%). As shown in Fig. 8, when the vibration stops, the vibration gradually decays. It shows that the higher the viscosity of the liquid, the faster the vibration decays.

We can get the mean value of decaying factor $\bar{\Lambda}$ by calculating the ratio of adjacent peaks and then solve β according to Equation (8). With β, we can further derive f_τ and then to estimate η. As shown in Fig. 6, the f_τ we calculated is very close to the theoretical f'_τ, and the mean relative error is 4.57%.

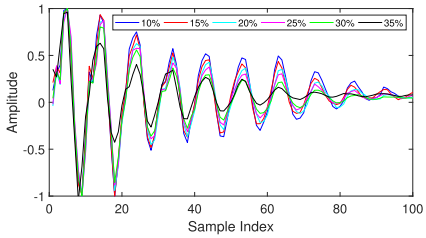

Fig. 8. Decaying-state of solution of different mass concentration after the motor stops moving.

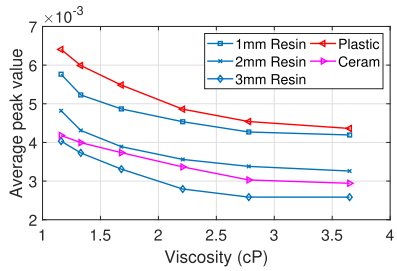

Fig. 9. The average peak value affected by the container's material and thickness.

3.6 The Impact of Container

In this section, we explore the interference brought by the container. We designed the experiments using containers of different materials (i.e., resin, plastic, and ceramic) in the same size. The containers were placed on the same table, filled with 400 mL sucrose solution in different concentrations, 10%, 15%, 20%, 25%, 30%, and 35%. We further explored the influence of container thickness, and utilized three different thickness resin containers (1 mm, 2 mm and 3 mm), and recorded the same volume and concentration sucrose solutions mentioned above. We recorded the relationship between the average amplitude of the accelerometer and the viscosity in Fig. 9.

Through experiments, we found that the container's wall material and thickness impact on the amplitude value. Different effects also occur on the curve slope when the container's wall material and thickness change. The result verifies that no matter how the container's wall shape and material change, as long as we can get the elastic coefficient constant value k of the container wall, we can eliminate the interference from different containers.

4 System Overview

Vi-Liquid is mainly composed of five modules, as shown in Fig. 10.

Parameter Calibration Module. Considering the errors between different mobile phones and containers, Vi-Liquid needs to calibrate and determine the parameters. By testing several viscosities known liquids, Vi-Liquid will calibrate the model's uncertain parameters through the known information. After the initial calibration, the model is ready for the testing of liquid.

Motion Detection Module. Considering the device's motion will interfere with the detected signal and cause misjudgement, we need to prevent the motion state when identifying the liquid. Therefore, we need to use Apple's motion recognition API "CMMotionActivityManager" [19] as the motion

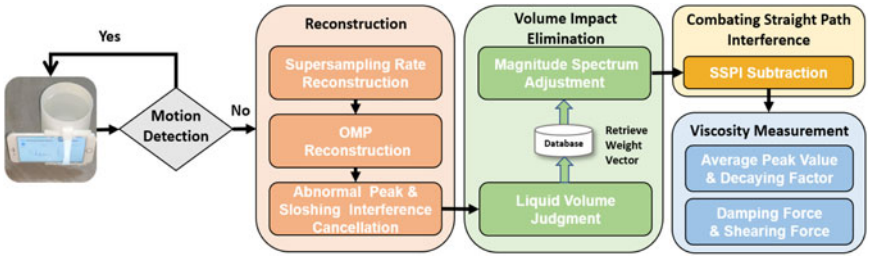

Fig. 10. The workflow of Vi-Liquid.

detection interface. This module divides the parameters returned by the API into two statuses, stable and unstable. When the module finds out the device is under an unstable scenario, the system would stop the detection process and wait until turning better.

Signal Reconstruction Module. By changing the interval time, Vi-Liquid applies *Supersampling Rate Reconstruction* Technique to reconstruct the signal. As the reducing sample, the signal is still rough and under-sampled. Then, Vi-Liquid utilizes the OMP algorithm to solve the pseudo-inverse matrix and converts the rough signal to the sparse domain. Further, Vi-Liquid eliminate the effects of abnormal peak and liquid sloshing interference.

Interference Cancellation Module. Vi-Liquid will utilize the rough signal obtained from the Signal Reconstruction Module to compare it with the recorded volume magnitude spectrum, and then judge by the threshold to get the liquid volume. Next, Vi-Liquid uses the volume weighting vector to eliminate the sparse signal volume interference. After that, Vi-Liquid combats the straight path interference by subtracting the the Standard Straight Path Interference (SSPI) .

Viscosity Measurement Module. Vi-Liquid needs to convert the volume-eliminated sparse signal into a time-domain signal. Then, Vi-Liquid combines the decaying factor, amplitude and other known parameters to calculate viscosity.

5 System Design of Vi-Liquid

This section illustrates the proposed solutions to the transmitter, propagation, and receiver side challenges when realizing the viscosity measurement on the smartphone.

5.1 Vibro-Motor Selection

In the previous section, we theoretically demonstrated the feasibility of estimating the viscosity of a liquid using vibration. Nevertheless, mobile phones utilize diverse vibration motors. In our pilot study, we found that not all the vibro-motor are applicable for the viscosity measurement using the vibration model we build in Section 2. According to the model, the vibro-motor should generate the shear strength on the liquid. Our implementation adopted the Linear Resonant Actuator(LRA) to generate the vibration, which is available for multiple commercial mobile phone including iPhone 7, 7P, 8, 8P, X and XR. However, because of built-in system protection in iOS, the motor can only vibrate continuously for 0.5 seconds. and then the motor vibration is forcibly paused by the phone for at least 0.25 s.

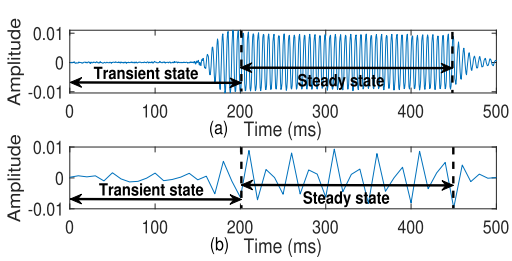

Fig. 11. The transient signal in different sampling rate. (a) 1600 Hz. (b) 100 Hz.

5.2 Mobile Phone Placement Selection

In the detection procession, we need an appropriate place to ensure that the vibration is efficient. We designed the experiment to find out the proper position. We set the phone's initial position of the experiments when the phone's home button's midpoint and the edge of the container card slot coincide, as shown in Fig. 12. This position can ensure the container's balance because continuing shifting to the left will cause the container to tilt due to beyond border of the phone's centre gravity and keep the motor at the bottom of the phone within the range of action. We shifted the phone to the right to detect the changes caused by the phone offset by 3 mm and 6 mm. We used the signal when there was no vibration as the noise, and calculated the signal-to-noise ratio received by the accelerometer at different positions. According to the amplitude value curve and the signal-to-noise ratio curve in Fig. 13, we found that when the mobile phone shifts to the right, it will cause the signal-to-noise ratio to drop. Also, the reduction of the measurement amplitude will reduce the viscosity range of detection. Therefore, we chose the position where the midpoint of the Home button overlap with the best signal-to-noise ratio coincides with the card slot's edge. Note that the vibro-motor is under the Home button of the mobile phone. As long as the mobile phone position shifts, the motor's torque force will be changed, thereby affecting detection accuracy. Therefore, we strictly controlled the placement of the mobile phone during the experiments.

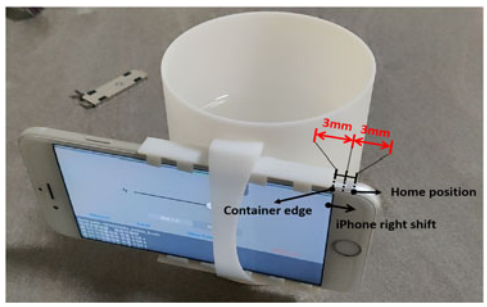

Fig. 12. The initial position and direction of phone placement.

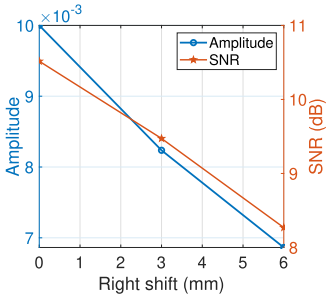

Fig. 13. The effect of amplitude and SNR in different phone placement.

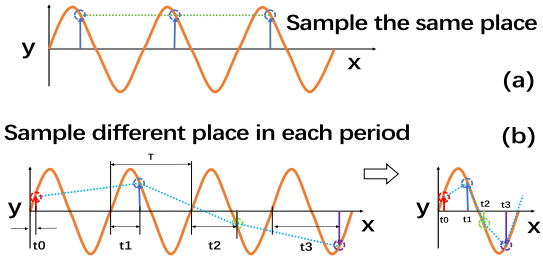

Fig. 14. The solution of undersampled rate. (a) The sampling rate is the same as the signal frequency. (b) The solution schematic of undersample rate.

5.3 Combating Straight Path Interference

In Section 3, we built an external circuit for feasibility study, which means means that we did not consider the straight path interference. The straight path interference implies that the vibro-motor's vibration transmits directly to the internal accelerometer rather than passing through the target liquid. The energy of straight path interference is significant, and the useful signal energy related to the viscosity is much lower than the interference. Therefore, we need to remove the straight path signal.

In order to understand the straight path interference, we need to use a high-precision accelerometer to sample the signal for analysis. We replaced the accelerometer chip in the iPhone 7 with a stand-alone accelerometer (BMI160) to record the vibration of straight path interference at 1,600 Hz sampling rate. It should notice that BMI160 is also used to assist in solving the observation matrix. Through the signal collected by BMI160, as shown in Fig. 11, we can observe a transient signal in the first 200 ms. Therefore, to eliminate the dirty signal in each detection, we will remove the first 200 ms transient signal.

What's more, we used a titration butterfly clip to suspend the phone in the air and record the vibration signal, because the soft contact points on the clip can absorb the vibration signal and prevent the reflection. We recorded the 300 ms steady-state vibration time-domain signal in 30 experiments and then performed a short-time fast Fourier transform with six 50 ms width segmented signals. We recorded the amplitude-frequency value of each segment and averaged the mode of each frequency point. These values will keep as the Standard Straight Path Interference (SSPI). Since the straight path's interference occupies the majority of signal energy, we have to scale the SSPI in the signal's frequency domain with interference. To eliminate interference, we subtract SSPI from the frequency domain of the segmented signals reconstructed by SRR and OMPR. After restoring the processed signal to the time domain utilizing the inverse Fourier transform, we will get the clean signal.

5.4 *Supersampling Rate Reconstruction* (SRR)

The accelerometer in iPhone 7 supports the sampling rate up to 1,600 Hz. Still, the maximum sampling rate is only 100 Hz through API due to the protection of iOS, which is much less than the vibration frequency of vibro-motor at around 167 Hz. According to the *Nyquist Sampling Law*, the low sampling rate results in the distortion of vibration waveform in the time-domain. The measurement error will increase because we apply the amplitude peak to estimate the parameters (see Section 2).

Because to realize this supersampling reconstruction method, the signal needs to have sufficient stability. To verify whether the signal stability, we put the two different resolution signals from Fig. 11, into the same time axis. By shifting the signal, we minimized the sum of variances of the corresponding points. We compared two signals, only 1.42% variance between them. Therefore, it is feasible to reconstruct the signal using the basic idea above.

Basic Idea of SRR.

To solve the low sampling rate problem, we apply the *Supersampling Rate Reconstruction*. As shown in Fig. 14a, when given a stable periodic signal, we might sample the same value if the sampling rate is too low and can not record the entire signal. If we can sample at a distinct time point in each period (e.g., start sampling after t_0, t_1, t_2, and t_3 in Fig. 14b) and record the timestamp, there will be plenty of sample points after several periods. Then we combine these sample points into one period and sort them by the timestamps. Finally, the re-ordered signal is comparable to the signal sampled at a high sampling rate. Above this is the basic idea of *Supersampling Rate Reconstruction*.

5.4.1 *Explore Reasonable Sampling Intervals*

When we perform the discrete Fourier transform on a signal, we will get

$$X(e^{j\omega}) = \sum_{n=1}^{N} x[t_n] e^{-j\omega t_n}, \tag{9}$$

where t_n , is the sampling time. When we substitute the t_n with any random number into the above formula, we can observe that the discrete Fourier transform will introduce random noise in the frequency domain, as shown in Fig. 15b. Then, we assume that time t_n obeys a uniform distribution, and its probability density distribution function is $p(t) = \frac{1}{T_{\max}}$, $t \in [0, T_{\max}]$ and $t \in [0, T_{\max}]$. We will get the spectrum expectations as

$$E[X(e^{j\omega})] = \frac{1}{T_{\max}} \sum_{n=1}^{N} \int_0^{T_{\max}} x[t_n] e^{-j\omega t_n} dt_n$$

$$= \frac{N}{T_{\max}} \int_0^{T_{\max}} x[t] e^{-j\omega t} dt = \frac{N}{T_{\max}} X(j\omega). \tag{10}$$

As shown in Fig. 15a is a 100 Hz non-uniformly spaced signal with 1,000 Hz sample rate. If t_n obeys uniform

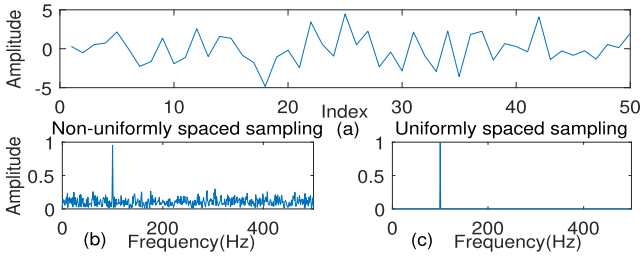

Fig. 15. The original signal and the magnitude spectrum obtained by sampling the original signal at different time intervals.

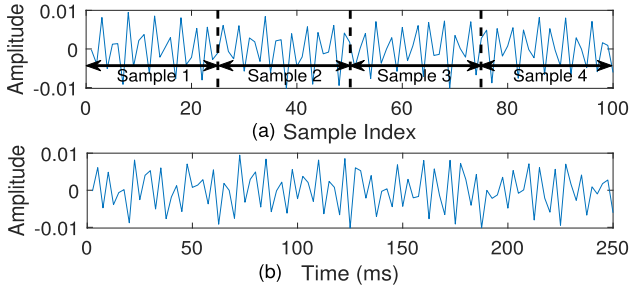

Fig. 16. We restore the vibration signal with Supersampling Rate Reconstruction.

distribution, the magnitude spectrum of uniform sampling is shown in Fig. 15c.

In the practical setting, a cycle composes of 0.5 s active vibration and a pause last for 0.5 s + $t_{wait} \times n_{th}$ cycle.

During the whole process, the accelerometer should keep sampling. After n cycles of sampling, we can achieve SRR for the signal reconstruction.

As shown in Fig. 16a, the under-sampled signal with 100 Hz sampling rate is considerably distorted. We set t_{wait} to be 2.5 ms, apply SRR for four cycles, and get the reconstructed signals as shown in Fig. 16b.

5.4.2 Explore Reasonable Re-Ordered Signal

Through observation, we found that when the mobile phone starts the motor, the electrical level is random(0 or 1), which may cause the critical problem - re-order the signal by inconsistent vibration directions. Because to re-order the n sets of randomness direction signals, it will produce 2^n combinations. If we do not make corrections, this will affect the accuracy of the re-ordered signal. We observed 50 reconstructed signal samples and compared the frequency spectrum of the re-ordered signal. In most cases, as Fig. 17 shows, we found that the correctly re-ordered signals have different proportional relations between the frequency domain's peak values. The highest peak in the correctly re-ordered signals will much higher than the other peak values, significantly more than two times larger than the second one.

What's more, the highest peak locates at the position around vibration frequency - greater than 150 Hz. It is because no matter how we re-ordered signal, the total power of the signal is consistent. However, the wrong re-ordered signal brings various frequencies of noise signals, distributing the total signal power. Second, there is a certain probability that the wrong re-ordered will lead to most of the points on the coaxial Y axis, which will bring energy-intensive low-frequency signals (because the wave fluctuation becomes slow down). Therefore, we set up a threshold (two times more distinguished than others compare with the highest peak), and in which larger than 150 Hz in frequency - to make a simple judgment to select the appropriate re-ordered signal result.

5.5 Orthogonal Matching Pursuit Based Reconstruction (OMPR)

Using the peak amplitude as a critical indicator will bring a severe shortcoming that requires a high sampling rate for signal acquisition. Because when the sampling rate is too low, it is difficult to obtain accurate peak amplitude information at the sampling point. If SRR is used to recover a signal with a high sampling rate, it will take much time. Therefore, we build based on SRR and further use OMPR to enhance signal resolution for improving efficiency.

We can confirm from the previous experiments vibration signals in the frequency domain shown in Fig. 17, the signal has fewer characteristic frequency points (non-zero points). We set up a threshold of 0.03 to remove the frequency points with inconspicuous features. At this time, the signal is sparse in the frequency domain. The original signal can reconstruct The signal characterizing with sparsity through a nonlinear reconstruction algorithm [20].

Because the high-sampled signal undergoes sampling matrix conversion and finally forms a low-sampled signal. The low sampling signal can express as

$$y = \varphi x, \tag{11}$$

where $x \in R^n$ and $\varphi \in R^{m \times n}$ is the the high sampling rate signal and sampling matrix. $y \in R^m$, $m << n$. We know that the original high-sampling rate signal has sparsity in the discrete Fourier transform domain, and the sparsified signal can be expressed as f.

$$y = \varphi\phi f, \tag{12}$$

where ϕ is an inverse transform operator. For the sake of simplicity, we represent $\varphi\phi$ as the observation matrix T. Therefore, we only need to find the smallest zero norm f that satisfies the condition of y. At this time, the 0-norm problem can be transformed into a 1-norm problem[20].

To obtain a suitable observation matrix T, we conduct the following experiment. We pour the sucrose solute in different mass (from 1 g to 500 g in a step of 1 g) into the water from 500 liquid samples. For all the samples, we record the vibration signal generated by vibro-motor using a standalone accelerometer (sampling at 1,600 Hz) and built-in accelerometer in the smartphone (sampling at 100 Hz), respectively.

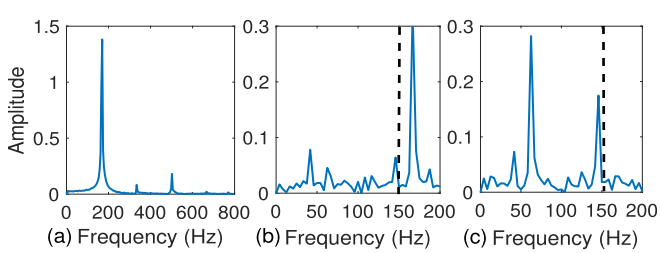

Fig. 17. The amplitude-frequency curve of the vibration signal. (a) The original signal received by the BMI160. (b) Correctly re-ordered signal. (c) Incorrectly re-ordered signal.

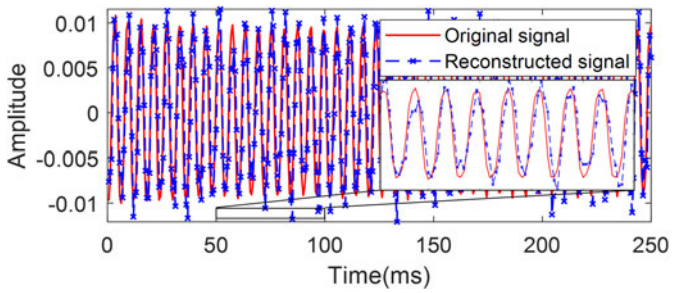

Fig. 18. A comparison of the reconstructed signal sampled by 4s and the original signal.

We reconstruct the low sampling rate signals to 167 Hz using SRR and denote the reconstructed signal as y_i. We consider high sampling rate signals as the original signal, and denote it as f_i. We substitute f_i and y_i into Equation (12) and obtain a multi-dimensional non-homogeneous linear equation. By solving the equation, we can get the observation matrix T.

Now, we know the observation matrix T. However, to complete the reconstruction, there is one last problem to be solved. Although we can get y during the measurement, it is a very complicated mathematical problem to solve the inverse matrix of the observation matrix T. Therefore, we need to use the pseudo-inverse matrix instead of the real value to solve. Specifically, we use the famous orthogonal matching pursuit (OMP) algorithm [21] to solve the inverse matrix. The OMP algorithm calculates the contribution values of the observation matrix T and y. It continuously updates the residual error for iterative convergence, and finally obtains the sparse signal f from the original signal. As shown in Fig. 18, we further restore the signal reconstructed by SRR to 1,600 Hz using the OMPR. Note that, if we use OMPR directly because the sampling rate of 100 Hz on the mobile phone is too low, the restored results are not good.

5.6 Abnormal Peak Noise Cancellation

Although we have reconstructed the signal, we found the signal still includes calculation bias. Through observations, we discovered that the reconstructed signal often has abnormal peaks, as shown in Fig. 19a. We found that these abnormal peaks have certain characteristics. For example, some peaks are lost and become jagged. This is the situation that most affects the amplitude calculation results, making the calculated average peak smaller and unstable. Therefore, we must eliminate this effect. On the other hand, we found that liquid sloshing causes the signal envelope to float up or down, interfering with the correct calculation of the amplitude. The envelope fluctuation will drift the mean value of the signal, also known as the direct current component (DC component). The DC component, also called the aperiodic component, often represents the signal fluctuation, as shown in Fig. 19a.

Empirical Mode Decomposition (EMD) [22] is an algorithm that decomposes signals based on the envelope and regards the oscillation within the signal as local. Therefore, it can well extract the abnormal peak feature. On the other hand, since EMD detailed steps are needed to calculate the mean value of the envelope, the DC component related to liquid sloshing can be extracted, and the liquid sloshing

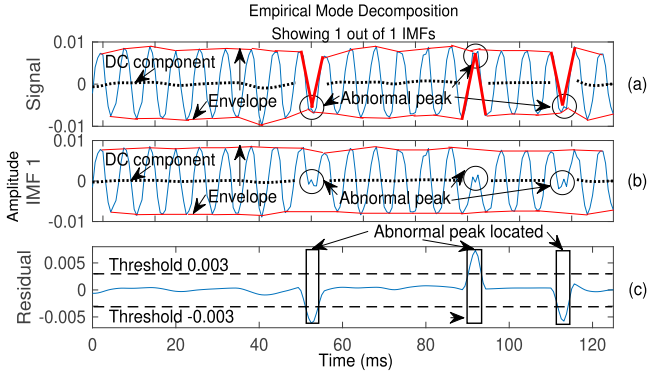

Fig. 19. The EMD decomposes once to identify false peaks.

interference can be eliminated by subtracting the DC component. In summary, we propose a method based on EMD to eliminate abnormal peaks and liquid sloshing interference simultaneously to make peak calculation more robust. First, we find the local maximum and local minimum points of the signal. The specific methods are

$$\begin{aligned} x_{max}\{x_1, x_2, \ldots, x_k\} &= max\{x_{i-1}, x_i, x_{i+1}\} \\ x_{min}\{x_1, x_2, \ldots, x_l\} &= min\{x_{i-1}, x_i, x_{i+1}\}, \end{aligned} \tag{13}$$

where $x_i \in x_{vib}\{x_1, x_2, \ldots, x_n\}$, is the ith sample index of the steady-state signal. Suppose k local maximum $x_{max}\{x_1, x_2, \ldots, x_k\}$ and l local minimum $x_{min}\{x_1, x_2, \ldots, x_l\}$ are found. Then, Piecewise Cubic Hermite Interpolation [23] is utilized to supplement $x_{max}\{x_1, x_2, \ldots, x_k\}$ and $x_{min}\{x_1, x_2, \ldots, x_l\}$ to the length of the steady-state signal n. Specifically, the first derivatives of x_{max} and x_{min} are calculated. Then, for two adjacent points, a polynomial $H_3(x)$ of which degree $\leqslant 3$ is constructed to satisfy the interpolation condition: the signal value and the first derivative are equal, respectively. After we get the all polynomials, we supplement x_{max} and x_{min}, denoted as upper envelope $u(t)$ and lower envelope $l(t)$ respectively. Note that we do not use cubic spline interpolation [24] for interpolation, because there is a big difference between the adjacent extremum values near the abnormal peak value. Cubic spline interpolation adds interpolation conditions with equal second derivatives, which is prone to signal overshoot, while Cubic Hermite interpolation can avoid this phenomenon.

Next, we calculate the mean value of upper and lower envelope ($m(t) = \frac{u(t)+l(t)}{2}$), which contains the DC component information related to liquid sloshing, as shown in the DC component in Fig. 19a. Next, we subtract it from the original signal to get the first Intrinsic Mode Function (IMF 1), where $IMF\ 1(t) = x_{vib}(t) - m(t)$. Note that we only do one decomposition, because one decomposition can ensure that the abnormal peak position is extracted precisely, and the abnormal peak in the residual is not diluted by multiple EMD decomposition. As shown in Fig. 19b, it is the signal after removing liquid sloshing interference. It can be seen that the DC component fluctuation decreases and the envelope becomes flat. Afterwards, the residuals were calculated ($res(t) = IMF\ 1(t) - x_{vib}(t)$), as shown in Fig. 19c. Note that since we only do one EMD decomposition, the calculated residuals are also the mean of the envelope. We consider that the location where the residual is greater than 0.003 is

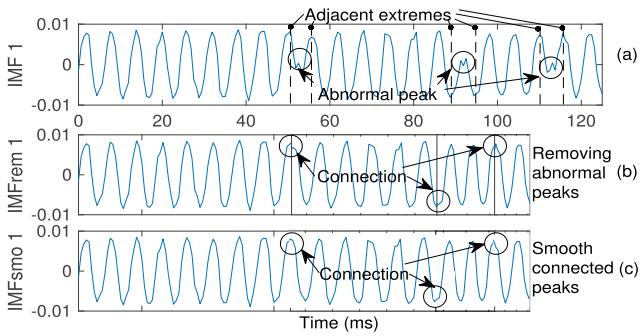

Fig. 20. Eliminate abnormal peaks from IMF 1.

the location of the abnormal peak. As shown in Fig. 20a, we first found the maximum or minimum values before and after the abnormal peak. Then, the abnormal peak is removed, and the signal IMFrem 1 after removing the abnormal peak is shown in Fig. 20b. However, since the two extremes at the connection are not necessarily the same, the average of the two extremes is taken as the new peak at the junction. Fig. 20c shows the signal IMFsmo1 after smoothing the connection. Finally, we calculate the average peak value of IMFsmo 1 as the amplitude of the steady-state signal.

5.7 Combating Volume Change Impact

Recalling the observation in Section 3.4, the liquid's volume change with the same viscosity causes different vibration readings. Suppose we measure the liquid viscosity with varying vibration readings using our proposed model. We will get different results if we measure the liquid viscosity with varying vibration readings using our proposed model, i.e., one kind of liquid in different volumes will have different viscosity, which is not tally with the fact.

5.7.1 Volume Weight Vector

In the experiment of Section 3.4, we found that if the container contains different volumes of liquid, then the steady-state vibration signal we receive will have a different amplitude-frequency curve. It is worth noting that the various volumes of amplitude-frequency curves are quite different. As shown in Fig. 21, the different viscosities liquids with the same volume showed similar magnitude spectrums on the left half. In contrast, the different volumes with the same viscosity showed diverse magnitude spectrums. We can observe that the volume influenced the magnitude spectrum's amplitude-frequency curve (the value of each column in the subfigure), but it is independent with the liquid viscosity. This results can be explained using our common sense, for example, tapping a tumbler with various volumes of liquid will hear different sounds. The main reason is that the liquid volumes will change the natural frequency of the entire system. Our idea is to weight the vibration signal results from different liquid volume and unify their amplitude to eliminate the volume impact. We use the 500 mL liquid as the reference liquid. In the magnitude spectrum, the amplitude of reference liquid at frequency bin i is ${a^{ref}}_i$.

The volume weight vector W_{volume} is defined as

$$W_{volume} = \left[\frac{{a^{vol}}_1}{{a^{ref}}_1}, \ldots, \frac{{a^{vol}}_i}{{a^{ref}}_i}, \ldots, \frac{{a^{vol}}_{800Hz}}{{a^{ref}}_{800Hz}}\right], \tag{14}$$

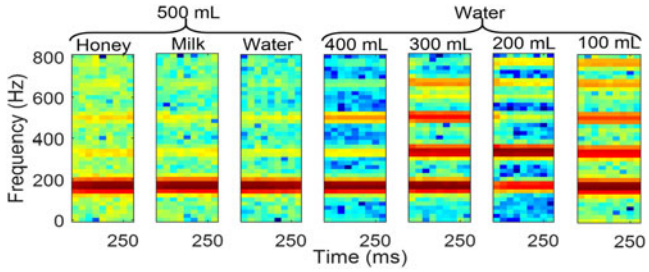

Fig. 21. The magnitude spectrum of liquids with different volumes and different viscosities.

where ${a^{vol}}_i$ indicates the amplitude at frequency bin i in the magnitude spectrum of a certain volume liquids.

5.7.2 Liquid Volume Estimation

However, we need to obtain the prior value of the liquid volume first and then apply the corresponding volume weight vector to the signal.

The container can be simplified as a cavity in the physical model. According to the Helmholtz vibration theory [25], the relationship between the resonance frequency f_r and the liquid volume V_l can express as

$$f_r = \frac{v}{2\pi}\sqrt{\frac{C}{V_l}}, \tag{15}$$

where v is the propagation speed of vibration, V_l is the liquid volume, and C is the conductivity of the container. As the liquid volume increases, the resonance frequency decreases. Therefore, we can now infer the liquid volume based on the frequency information. Specifically, we calculated the magnitude spectrum based on IMFsmo 1 and obtained frequency deviation information. The relationship between the frequency and liquid volume can be learned and stored in the database in advance. Therefore, we can now get the liquid volume V_l by matching the samples in the database.

Combining the method in the previous section, we eliminate the interference caused by different volumes. As shown in Fig. 22, using super-resolution reconstruction signals for different volumes, the curves obtained are very similar, and the residual of least square is only 0.023.

5.8 Damping Coefficient Error Correction

In Section 2.2, the model has introduced the decaying factor, which is used to calculate the damping coefficient β. However, using the peak value after SRR in the decaying-state introduces errors, because the sampling rate of 400 Hz can not cover every attenuation peak. More importantly, OMPR

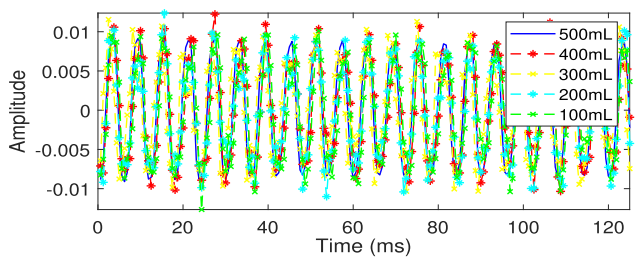

Fig. 22. Use super-resolution to reconstruct signals for different volumes.

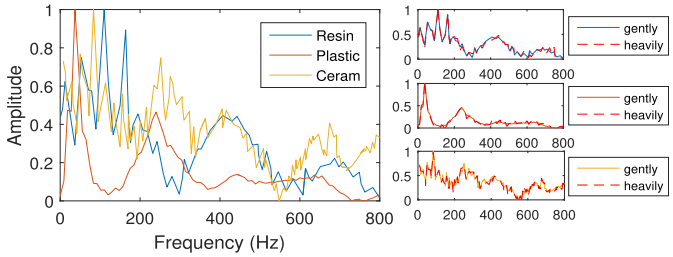

Fig. 23. The amplitude-frequency curves from tapping in different tap forces on various material surfaces.

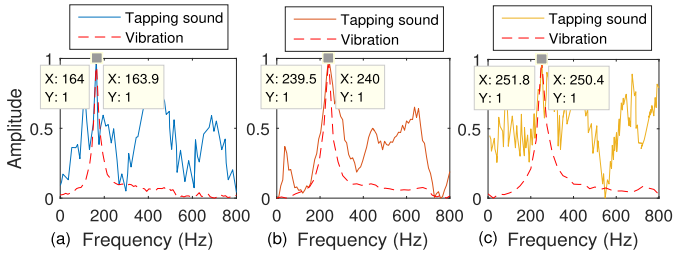

Fig. 24. Different materials containers have the approximate largest amplitude as the transformed amplitude-frequency curve of vibration signals and tapping sound signals in the decaying-state. (a) Resin. (b) Plastic. (c) Ceram.

is not suitable for recovery of signals with decaying motion, because the frequency and amplitude attenuation rates vary with the liquid damping.

In order to reduce the error of the damping coefficient calculation, we need to find a more accurate damping coefficient estimation method.We need to design a solution that can not only remove the error but also do not cause trouble to users. Suppose we could use the curve fitting to calculate the equation of vibration under the decaying-state. After that, we will obtain an accurate damping coefficient. However, although the theoretical function has been given in Equation (7), it is necessary to know some parameters if we want to realize it through the fitting method. That is because too many unknown parameters will lead to multiple fitted curve results and make it difficult to choose an appropriate one.

Regarding that, after the vibro-motor stops moving, the vibration generated during the decaying-state is a damping movement. That means the mobile phone vibrates under the action of inertia and is subjected to the container material and liquid resistance then gradually stop the movement. Through Equation (7), we can see that $\sqrt{\frac{k}{m}}\sqrt{1-\left(\frac{\beta}{2\sqrt{km}}\right)^2}$ is the vibration frequency of decaying-state. Observing the experimental results in Fig. 8 shows that the mobile phone is subjected to under-damped motion in the decaying-state.

However, the natural frequency of general solids is much higher than the iPhone's accelerometer sampling rate. Therefore, we seek a new way to measure the natural frequency rather than the accelerometer. Considering that the microphone sampling rate can reach 48 kHz, we hope to use the microphone's high sampling rate to obtain the natural frequency of container holding liquid. The vibration signal and sound signal of different materials after tapping have similar spectrum, and the location of local peak associated with the material is the same[26], [27]. Therefore, we tapped three containers made of different materials: resin, plastic, and ceramic, and then collected the sound signals. In the experiment, we tapped the same position, located at the top of the rightmost slot. We chose this location mostly because it is where the vibro-motor works at, and the natural frequency calculated will be more appropriate. As shown in Fig. 23, we found that the three different materials have their unique amplitude-frequency curves regardless of the tapping strength on the surface. However, we found that the low frequency of the tapping sound has a large energy, showing the shape of a logarithmic curve [28]. This is due to the phenomenon of sound dispersion, which leads to the slow propagation speed of low-frequency sound, and further leads to the superposition of relatively large energy of low-frequency part [29]. In order to eliminate the shelter of low-frequency energy, we made the following transformation to the signal:

$$S_{log}(f) = S(f) \times log_e\left(\frac{f}{max(f)} + 1\right), \tag{16}$$

where $S(f)$ is the original sound frequency amplitude spectrum, f is the frequency index, and $e(e \approx 2.7)$ is the base of the natural logarithm. On the other hand, we used a high sampling rate accelerometer to record decaying-state vibration signals of containers with different materials. Then we compared with the transformed vibration signals' and the tapping sound signals' amplitude-frequency curve. As shown in Fig. 24, we found that for containers of the same material, the largest peak frequencies of the two signals are very similar.

Therefore, taking advantage of these characteristics, we propose the Damping Coefficient Error Correction method. When user testing liquids, he/she should tap the top of the rightmost slot. This newly adding step is friendly to users and easy to operate during the detection. The system will choose the largest peak frequency in the tapping sound signal as damping vibration frequency to calculate the damping coefficient. Next, the system will substitute the peak amplitude of SRR and OMPR as A to fit the low-resolution sampled signal. It will change the exponential term and phase's value and use the least square method's optimal solution as the fitting function's optimal solution. Finally, the system will utilize the exponential term obtained by the fitting function to solve the damping coefficient β.

5.9 System Calibration

To make the system more ubiquitous, we need to consider several conditions, such as container materials, and differences in COTS devices. Considering the system's errors, which may be caused by slight differences in mobile phones or subtle changes in the container's wall material, we found it necessary to calibrate before using the system.

First, we need to consider the material of the container. The material of the container determines the elastic coefficient k and therefore affects the vibration signal. Next, we need to take the differences of the COTS devices into account. In order to explain the possible reasons for the differences, we use the motion equation [30] to represent the vibration generated by the mobile phone and the vibro-motor. When the phone vibrates, we can represent the phone's and the vibro-motor's coordinates as $x_1(t)$ and $x_2(t)$ respectively. The motion equation is given as follows:

$$M\frac{dx_1(t)^2}{dt^2} + c_0\left(\frac{dx_1(t)}{dt} - \frac{dx_2(t)}{dt}\right) + k_0(x_1(t) - x_2(t)) = -F\sin(\omega_0 t) \quad (17)$$

$$m\frac{dx_1(t)^2}{dt^2} - c_0\left(\frac{dx_1(t)}{dt} - \frac{dx_2(t)}{dt}\right) - k_0(x_1(t) - x_2(t)) = F\sin(\omega_0 t). \quad (18)$$

Among which, m is the phone's mass, M is the mass of the vibro-motor. c_0 and k_0 are respectively related to the phone's internal structure. F and ω_0 are respectively the magnetic force generated by the vibro-motor and vibration frequency. Therefore, the mobile phone's straight path is related to the phone's internal structure. We perform Laplace transform on Equations (17) and (18) and multiply s^2, $X_1(s)$ and m to get the phone corresponding external force

$$s^2X_1(s)m = \frac{-mMs^2F\omega_0}{(mMs^2 + c_0ms + c_0Ms + k_0m + k_0M)(s^2 + \omega_0^2)}, \quad (19)$$

where $X_1(s)$ is the Laplace transform of $x_1(t)$ and s is complex frequency. Equation (19) shows that the external force f_0 of COTS device is related to mass and internal structure. Since different COTS devices may have differences in mass and structure, calibration is necessary before identification.

Note that the impetus of different mobile phone motors varies, we compared the four types of mobile phone, and observed the vibration signal. However, the curve slope of the liquid was independent of the impetus. We tested four common liquids with known viscosity (η_1, η_2, η_3 and η_4). We selected standard liquid distilled water, 5%, 10% and 20% pure sucrose solution. Each liquid had four volumes, ranging from 100 to 500 mL, and a 100 mL gap between each calibration. We input these four viscosities into the system. According to Equations (2), (5) and (8) , we could complete the calibration of the parameters k, m, f_0 and $S_0\frac{v}{x}$ by solving the following Simultaneous Equations:

$$\begin{cases} \eta_1 = E\left(k, m, f_0, S_0\frac{v}{x}\right) \\ \eta_2 = E\left(k, m, f_0, S_0\frac{v}{x}\right) \\ \eta_3 = E\left(k, m, f_0, S_0\frac{v}{x}\right) \\ \eta_4 = E\left(k, m, f_0, S_0\frac{v}{x}\right) \end{cases}. \quad (20)$$

6 System Evaluation

6.1 Experiment Setup

In the following experiments, we deployed the iPhone 7 in the side slot of the 3D-printed container to measure the viscosity, as shown in Fig. 1. The vibration frequency of vibro-motor was 167 Hz, and the accelerometer's sampling rate was 100 Hz. The difference in waiting time t_{wait} was 2.5 ms, and we stopped sampling after the motor restarts four times. We utilized viscometer $ATAGO - VISCO^{TM}$ 895 for ground truth measurement. We repeated each measurement for 10 times and obtained the mean value. The rest of the settings was the same as that in the feasibility study.

TABLE 1
Measuring Viscosity for Various Liquids With Vi-Liquid and Viscometer (± shows std. GT for ground truth)

Liquid	β	$f_{\tau(N)}$	Vi-Liquid(cP)	GT(cP)	Error(%)
5%salt solution	0.8775	0.0134	1.03±0.019	1.00	3.00
10%salt solution	0.8757	0.0142	1.09±0.019	1.07	1.87
5%sucrose solution	0.8760	0.0140	1.08±0.025	1.06	1.89
10%sucrose solution	0.8745	0.0155	1.19±0.031	1.16	2.59
Coffee(10g sugar)	1.3770	0.0498	3.83±0.194	3.78	1.32
Coffee(15g sugar)	1.4392	0.0525	4.04±0.094	3.94	2.53
Coffee(sugar-free)	1.3566	0.0489	3.76±0.169	3.65	3.01
Whole milk	0.8980	0.0218	1.68±0.119	1.75	4.00
Skim milk	0.8745	0.0156	1.20±0.075	1.26	4.76
Yogurt	55.545	2.0887	159.14±4.800	152.45	4.39
Beer	0.8748	0.0148	1.14±0.013	1.11	2.70
Chinese liquor	0.8745	0.0155	1.19±0.031	1.23	3.25
Coca-Cola	0.8747	0.0149	1.15±0.019	1.13	1.77
Pepsi-Cola	0.8745	0.159	1.22±0.013	1.24	1.61
Chocolate liquor	14.888	0.5625	43.28±0.756	40.06	3.22
Honey	1009.8	37.899	2815.28±58.88	3000.12	6.16
Sweet tea	0.8751	0.0166	1.28±0.025	1.32	3.03
Green tea	0.8782	0.0131	1.01±0.019	1.03	1.94
Pineapple juice	33.245	1.2518	96.29±3.78	100.02	3.72
Tomato juice	28.015	1.0555	81.19±1.45	79.03	2.73
Vinegar	0.9393	0.0261	2.01±0.056	2.05	1.95
Soy sauce	0.9799	0.0292	2.25±0.113	2.18	3.37
Soya bean oil	21.145	0.7976	61.35±0.756	59.29	3.47
Vegetable oil	10.214	0.3870	29.77±0.644	30.94	3.78
Lard oil	19.233	0.7258	55.83±0.756	53.18	4.98
Oil(light)	39.047	1.4695	113.04±1.906	108.49	4.19
Oil(heavy)	231.24	8.6821	684.31±3.325	658.12	3.98
Disinfected alcohol	0.8809	0.0189	1.45±0.075	1.42	2.11
Glycerol	273.09	10.253	788.67±4.800	800.45	1.47
Laundry detergent	70.319	2.6432	203.32±2.331	201.05	1.13

6.2 Liquid Identification Performance

To verify the effectiveness of our proposed model and techniques, we first used our system to measure the viscosity of 30 kinds of liquid (500 mL) and compared the estimated results with the ground truth. As shown in Table 1, the liquids we chose are common in daily life, including beverages with different formulas. We also estimated liquids with different salt, sugar, and fat concentrations. In addition, we selected some readily obtained dangerous liquids as test samples as well.

6.2.1 Baseline Accuracy

We report the estimated viscosity for 30 different liquids in Table 1. Through the results, we notice that Vi-Liquid is effective in measuring viscosity. Comparing to the ground truth, the mean relative error of our system is 2.3%. By taking the estimated viscosity as features, ground truth as labels, we can adopt a simple K-Nearest Neighbors algorithm (K = 1) to differentiate those liquids. Fig. 25 presents the resulting confusion matrix, which shows an average classification accuracy of 97.33% for 30 kinds of liquids. Evidently, Vi-Liquid can distinguish a large number of liquids correctly, even if they are highly similar, like Coke and Pepsi.

6.2.2 Comparison With the Latest Researches

Here, we compare the liquid identification performance of Vi-Liquid with the latest researches. The objects for comparison are TagScan [1] (RFID, 10 types of liquids), Smart-U [3] (LED, 6 types of liquids), and WiMi [31] (Wi-Fi, 10 types of liquids). We modified the experiment setup to control the type of liquids and the number of repeated measurements

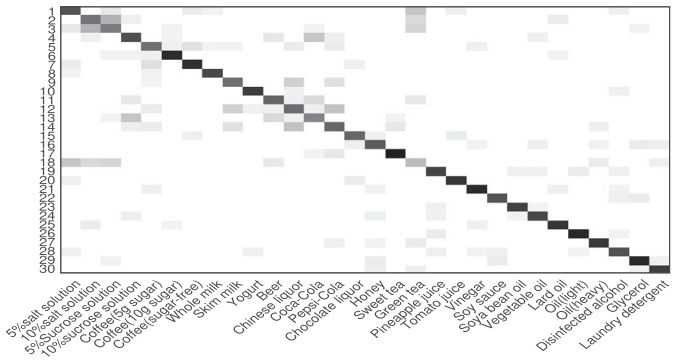

Fig. 25. Confusion matrix for liquid identification with estimated viscosity.

TABLE 2
The Accuracy Performance of Vi-Liquid and the Latest Researches

Item	Accuracy	Item	Accuracy	Item	Accuracy
Vi-Liquid	97.67%	Vi-Liquid	98.00%	Vi-Liquid	98.33%
TagScan	98.20%	Smart-U	93.00%	WiMi	96.00%

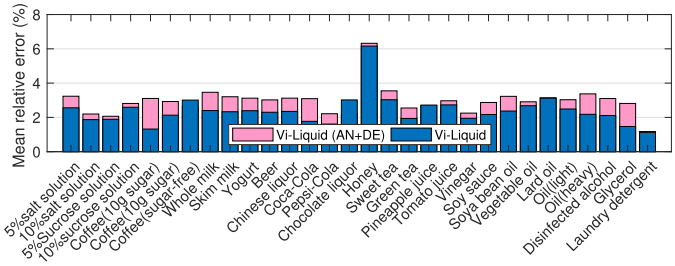

Fig. 26. The improvement of using Abnormal Peak Noise Cancellation and the Damping Coefficient Error Correction steps.

in order to be consistent with the objects for comparison. Table 2 shows the performance of Vi-Liquid compared with the latest researches, and Vi-Liquid outperforms Smart-U [3] and WiMi [31]. Note that although TagScan [1] has a 98.2% accuracy rate, which is slightly higher than 97.67% for Vi-Liquid, TagScan [1] requires additional commercial RFID device at the cost of around $1000. On the contrary, Vi-Liquid utilizes the ubiquitous phone and a 3D-printed container to reach a similar level.

6.2.3 Impact of Abnormal Peak Noise and Damping Coefficient Error

The Abnormal Peak Noise and the Damping Coefficient Error will cause a high bias in the identification accuracy. To show the difference in the accuracy, we process the signal in two different ways. One of them was to accomplish the noise elimination steps by steps ultimately. The other was to ignore the Abnormal Peak Noise Cancellation step after signal reconstruction and then ignore the Damping Coefficient Error [32]. We label the unapplied one as Vi-Liquid (AN+DE). The applied of Abnormal Peak Noise Cancellation and the Damping Coefficient Error Correction steps had decreased the mean relative error by 0.61%, as shown in Fig. 26.

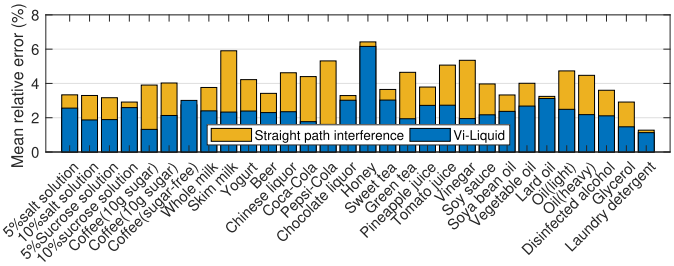

Fig. 27. The estimated viscosity errors of the signals with the straight path interference.

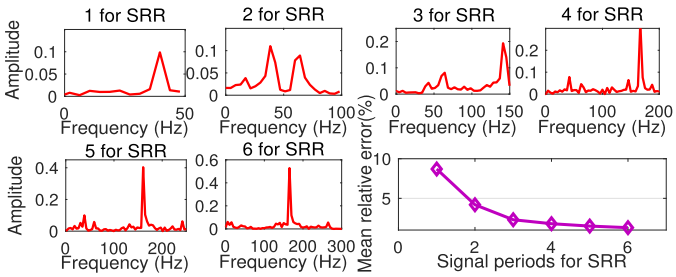

Fig. 28. Frequency spectrum of SRR signals of different periods and mean relative errors of using different periods signal to estimate the viscosities.

6.2.4 Impact of Straight Path Interference

Due to the straight path interference from the motor to the accelerometer, the low SNR boosts the measurement deviation. In Fig. 27, we can see the mean relative error without removing the straight path interference is 3.96% which is much higher than the baseline. This comparison shows the necessity of eliminating the straight path interference.

6.2.5 Impact of the Number of Periods for SRR

When the number of distinct periods of the periodic signal is different, it will affect SRR result. Furthermore, as the original signal that is used for OMPR, it will further impact reconstruction result. As shown in Fig. 28, we found that when the number of periods of the periodic signal for SRR became more, the frequency of the SRR signal became sparser and the mean relative errors were lower. The result shows that one period signal is difficult to reconstruct and causes significant error. However, as the number of periods increases to 4, the mean relative error decreases no longer significantly.

6.2.6 Impact of OMPR

The low sampling rate (400 Hz after SRR) will generate a sampling deviation caused by waves superposition and phase change. It will cause considerable errors in fine-grained analysis. We utilized OMPR mechanism to restore the under-sampled signal to a high sampling rate and decrease the mean relative error by 1.99%, as shown in Fig. 29.

6.2.7 Impact of Volume

In this experiment, we measured the viscosity of water, milk, and orange juice in different volumes (i.e., 100 mL, 200 mL, 300 mL, 400 mL, 500 mL) without weighting the signal. We can see from the results shown in Fig. 30 that the unweighted

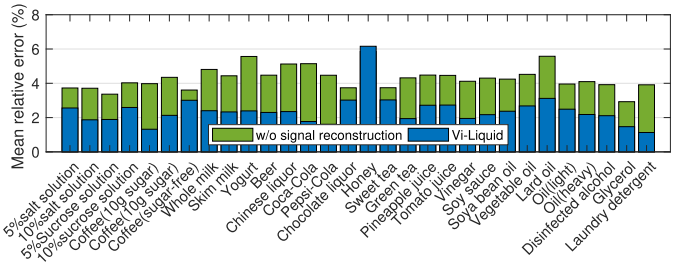

Fig. 29. The mean relative errors of using the original signals to estimate the viscosities.

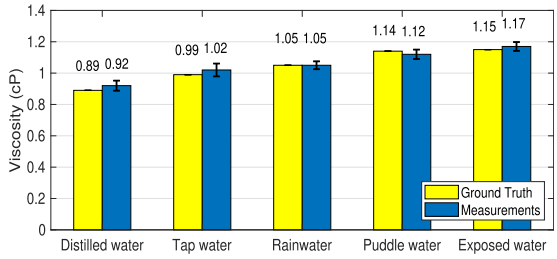

Fig. 31. Water contamination detection.

group produces large and unacceptable estimation variation and error. After we set the weight based on the analysis of the amplitude-frequency diagram discussed in Section 5.7, we can eliminate the influence results from the volume variation; hence the measured viscosity of the same liquid in different volumes is constant.

6.3 Water Contamination Detection

Drinking non-potable water often results in severe consequences, such as fever, diarrhea, retching, or even death sometimes. The common non-potable water includes tap water, rainwater, puddle water, and water exposed to the air for a long time; they have subtle differences. Tap water always contains organic compounds, heavy metal ions, and residual disinfectant; rainwater carries much atmospheric dust. And puddle water always mixes with large suspended particles. The water exposed for a long time in the air will breed a large number of bacteria and contains unknown secretions.

In this experiment, we aim to validate that our system can distinguish the subtle differences in the above mentioned five water sources by measuring viscosity. The estimated viscosity of the water sources mentioned above demonstrates in Fig. 31. The mean relative error is 2.33%, which indicates that if the unknown liquid's viscosity is higher than that of potable water by 0.1 cP, we can be confident that the unknown liquid is non-potable. Among different water sources, distilled water and tap water have the smallest difference in viscosity. Although the difference is only 0.1 cP, it is sufficient for the users to judge if the water has a contamination sign. Therefore, Vi-Liquid can help the area with limited sanitary water facilities detect the water contamination effectively.

6.4 Urine Composition Discrimination

Common causes of kidney disease [25] are bacterial infections, high blood pressure, and diabetes. When kidney disease occurs, glomeruli filter function or renal tubule reabsorption function degrades, causing the uric acid and protein to leak into the urine. Therefore, the uric acid and protein concentration in urine is an important indicator of kidney function damage and many other physiological diseases. However, to find out the kidney disease through the general urine test requires patients to go to the hospital themselves. It is inconvenient and prevents many patients from getting timely medical treatment. We hope that Vi-Liquid can help people monitor their uric acid and protein levels in urine at home using just a mobile phone. In this way, people can adjust their physical activity and eating behaviors to avoid the deterioration of the disease, or they can seek a doctor for medical examination in time when the protein levels exceed a safe threshold.

Since it is hard to control urine substances, we synthesized artificial urine by mixing distilled water and quantitative urea (agricultural nitrogen fertilizer) according to the urea content of a healthy person at 38 mg/100mL. We then poured different levels of sodium urate and ovalbumin powder into the artificial urine, respectively, to form the urine sample with different uric acid and protein concentration. Fig. 32 gives the urine viscosity level with the increase of uric acid and protein concentration. The mean absolute error is 1.13 mg/100 mL for uric acid and 0.18 mg/100 mL for protein. Note that the patient typically has the nephritis if the concentration of uric acid is higher than 60 mg/100 mL [13] and the complication of microalbuminuria if the concentration of protein is higher than 3 mg/100 mL [14].

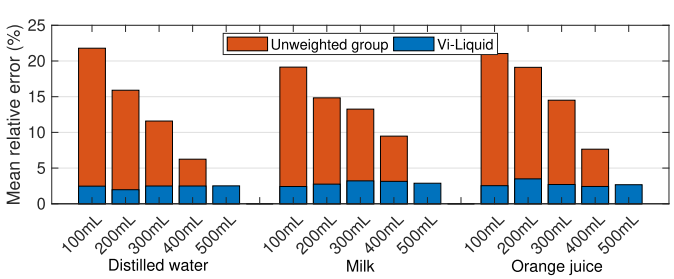

Fig. 30. Comparing the changes in viscosity measurement before and after using the volume elimination method.

6.5 Alcohol Concentration Measurement

Ethanol solution is a mixture of ethanol and water. The viscosity of ethanol is higher than water. Intuitively, the viscosity of ethanol solution increases with a higher concentration level of ethanol. With the help of Vi-Liquid for measuring ethanol concentration and volume of alcohol drinks, people can monitor their daily amount of ethanol intake with a mobile phone, thereby avoiding health risks, dangerous driving, and drug toxicity. The relationship between measured viscosity and ethanol concentration is plotted in Fig. 32. The result shows that Vi-Liquid can accurately estimate the ethanol concentration with an mean absolute error of 1.38 mass %.

6.6 Robustness

In Robustness research, we need to use different mobile phones to observe the error after calibration. Simultaneously, to verify whether the system can adapt to containers of different materials or thickness, we also need to compare the identification results when using different material containers or to

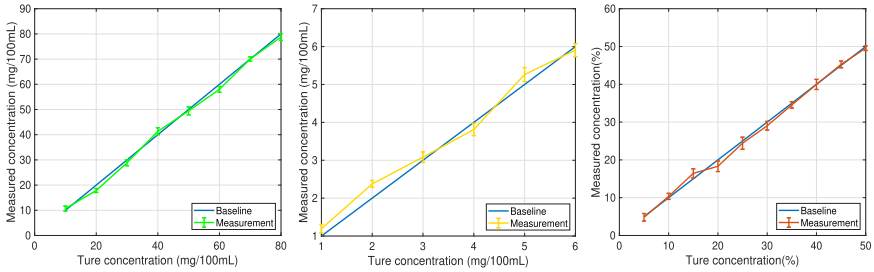

(a) Sodium urate (b) Ovalbumin (c) Alcohol

Fig. 32. Concentration level estimation based on viscosity.

use different thickness. We further placed the container in different experimental environments to test the anti-noise capability of the system.

6.6.1 Mobile Phone Type

First, we chose three types of iPhone (i.e, iPhone 8, iPhone X, and iPhone XR) to test. Then we printed the resin container with the same size as the previous one, but with different slots to fit the size of phone. Next, we calibrate in advance as described in Section 5.9, because the structure and container of the phone will affect the parameters of the system. As shown in Fig. 33, different mobile phones can keep low error after calibration. Their mean relative errors for 30 liquids were 2.3%, 3.3% and 3.9%, respectively.

6.6.2 Material and Thickness of the Container

We printed containers of different materials (i.e, resin, plastic, and ceramic) but the same size as the container mentioned earlier. We further explored the influence of container thickness, and printed three different thickness resin containers (1 mm, 2 mm and 3 mm). After calibration according to Section 5.9, we calculated the mean relative errors for 30 liquids. It can be seen from Fig. 34 that different container materials and thickness do not signally affect the liquid testing after calibration.

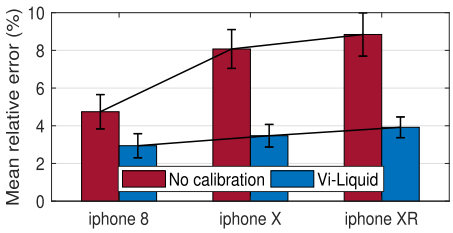

Fig. 33. Using different mobile phones to observe the errors after calibration.

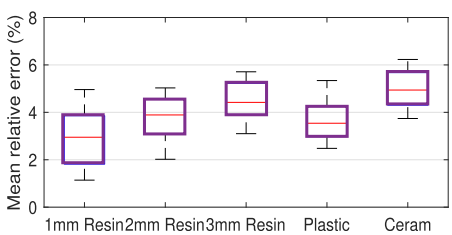

Fig. 34. The result of different material or sizes of containers.

6.6.3 Different Environments

We tested in four environments (i.e., quiet laboratory, supermarket, subway and airport), where environmental noise levels vary, ranging from 50 to 97 dB. Fig. 35 illustrates that the system still works well in noisy environments, as it is unlikely that voice travelling through the air will have any noticeable effect on accelerometer [33]. The low mean relative errors which are less than 3.5% in the four environments indicate that our system is robust.

6.7 The Boundary of Measurement

We noticed that Vi-Liquid has a relatively high error of 6.16% when measuring honey of 3,000 cP. We speculated that when the viscosity coefficient is higher, the difference in the shearing force generated by the vibrating liquids to the cup wall is more difficult to reflect in the vibration reading. Therefore, in this experiment, we explored the upper boundary for viscosity measurement in Vi-Liquid. We define the available upper boundary as the time when the estimation error exceeds 5%. As shown in Fig. 36, honey is a typical liquid that exceeds the upper measurement boundary of Vi-Liquid. We diluted the honey with water to reduce its viscosity until the measurement error is near 5%. At this point, we regard that 2,500 cP as the upper boundary using Vi-Liquid.

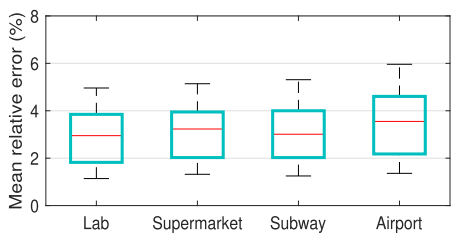

Fig. 35. The result of placing the container in different experimental environments.

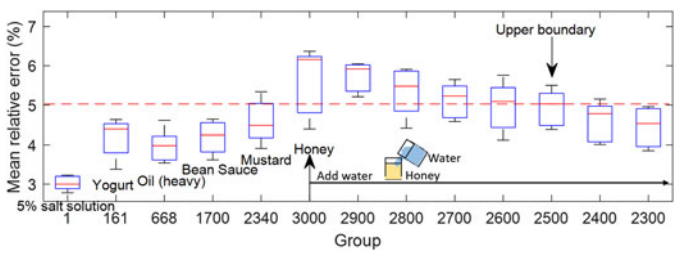

Fig. 36. Explore the boundary of viscosity measurement of our system.

7 Related Work

7.1 Ubiquitous Liquid Testing

Recent research on ubiquitous liquid testing has given a large number of different problem-solving theories and meaningful applications. They mainly lies in two categories, namely RF-based [1], [2], [4], [34] and optical camera based [3], [5], [6], [35].

RF-Based Systems. The RF-based systems mainly exploits the radio signal propagation characteristic inside the target liquid to identify liquids. TagScan [1] extracts the RSSI and phase change as features from RFID tag reading and classify 10 liquids. LiquID [4] uses two independent ultra-wideband (UWB) units to estimate liquid's actual permittivity, which scales the identification of liquid type to 33. RFIQ [2] and TagTag [34] propose to attach one RFID tag on the target of interest for liquid testing. They achieve the detection of fake alcohol, baby formula adulteration, fake luxury CHANEL perfume and expired milk by comparing with the training set. Mm-Humidity [36] uses millimeter waves to measure the liquid content in the air. However, their approach can not predict the concentration level and requires a complicated setting (i.e., an RFID reader in [1], and a large container in [4]).

Optical and Camera Based Systems. Thermal infrared sensor, photodiode and visible light camera are widely used as a photodetector to acquire the information about optical absorption or reflection of liquid. It is easy to reveal the liquid property by analyzing the optical spectra. In Nutrilyzer [5], a photoacoustic sensing system was proposed. It leverage the modulated shining light of various wavelength to travel through the liquids and produce unique spectra for characterizing the nutrients and adulterants in liquids. By employing the LEDs and photodiodes, Smart-U [3] is able to recognize food or liquid in the spoon because the diversity of substances in foods will affect the absorption spectrum. Allight [35] propose a smart ice cube device equipped with near-infrared and visible LEDs, which can estimate the alcohol concentration level of beverages by utilizing the near-infrared spectrometry principle. Lili [37] is the latest technology. It proposes a valuable system that uses LEDs and photodiodes to achieve finer granularity, which can be used to measure capillary waves and microbial composition changes in liquids. However, these proposals rely on the extra specialized device for liquid testing, typically unavailable for general users. On the other hand, Vi-Liquid is a smartphone-based liquid testing system that supports multiple applications simultaneously.

CapCam [6] is the first mobile application that can measure liquid surface tension. It leverages the smartphone's vibro-motor to generate capillary waves on the liquid surface and capture the light pattern on the container's bottom using the flashlight camera. However, it is not able to identify unknown liquids and fail to function in testing opaque liquids. In contrast, Vi-Liquid measures the liquid viscosity coefficient through vibration signals, based on supporting all applications of CapCam [6], it can also identify different liquid types without training.

7.2 Measuring Liquid Viscosity

Liquid viscosity testing is one of the main methods to analyze liquid constituents. For example, soil exudate's viscosity [38] will discover the pollutant components, and blood viscosity detection [7] can determine the content of cholesterol deposits. Earlier works, the capillary viscometer [8], the cylindrical torsional viscometer [9] the falling ball viscosity method [12] calculates the liquid's viscosity from Fluid Mechanics.

The cantilever beam liquid analyzer [10], [11] applies a cantilever inserted into the liquid to analyze cantilever shaking. [39] used a 3D printed parallelogram flexure hinge structure and optical fibre to replace the traditional system parts, which improved the invasive method's detection accuracy. However, they all need to use very sophisticated instruments, professional researchers to operate and invasive methods. There are not suitable for general beverage identification, and especially the unhygienic devices may lead to contagion risks. Employing the ultrasonic waves is a non-invasive way. Ultrasonic waves will generate the surface waves [40] directly correlated with the viscosity of liquids. Moreover, the reflection signal [41] also shows the relationship with viscosity. However, demanding liquids to be exposed to the air limits their application scenarios. The application of the photothermal effect [42] to detect the heat capacity ratio relative to viscosity requires a sophisticated and expensive thermal imager. The Brillouin scattering method [43] utilizing light can quickly obtain the viscosity of the liquid, but the ultra-wide bandwidth spectrum and the precise optical path detection equipment largely increase the detection overhead. Vi-Liquid only employs a smartphone, a readily accessible device, for the non-intrusive viscosity measurement. The systems can be operated by just a single click of the user. Therefore, Vi-Liquid is more suitable for the user to test the liquid in daily life. Even if compared with [32], we still have a great improvement in identification accuracy.

7.3 Vibration-Based Applications

Recent years have witnessed the rapid development in vibration-based sensing applications, benefiting from vibration signals' excellent properties. A large variety of novel proposals using vibration signals are presented, ranging from keystroke recognition [44], [45], human activity monitoring [46], [47], user authentication [48], [49], [50], gesture recognition [51], [52], and nearo-field communication [53]. Because the vibration generator and the receiver (i.e., vibromotor and IMU) is universally embedded in wearables and mobile phone, it is convenient for the researchers to leverage vibration signals for mobile computing. Oinput [45] and VibID [50] leverage passive and active vibration for identification, respectively. TouchPass[49] builds a behavior-irrelevant on-touch user authentication system on smartphones.

Different from these work, Vi-Liquid extends the kinematics equation of single-degree-of-freedom and combines it with the viscosity theory to build a liquid viscosity testing system. It can effectively identify unknown liquid, detect water contamination, monitor alcohol intake, and measure the uric acid and protein concentration in urine.

8 Conclusion and Future Work

This paper proposes Vi-Liquid, a liquid testing system that can accurately measure the liquid viscosity using vibration

signals on smartphones. We establish a novel calculation model that links vibration with viscosity and validate the feasibility on a smartphone. To break the system restriction, we found the proper *Supersampling Rate Reconstruction* and employ OMP reconstruction to restore the undersampled signal. Further, we cancel the straight path interference and volume change impact to improve the system performance. Our comprehensive experiments show that Vi-Liquid can successfully identify 30 kinds of unknown liquids, detect the water contamination, monitor the alcohol intake, measure the concentration level of uric acid and protein in the urine. We envision that Vi-Liquid can serve as a satisfactory assistant for ubiquitous liquid testing in many realistic application scenarios.

However, as a proof-of-concept prototype for liquid viscosity measurement, Vi-Liquid still has some limitations to be addressed in our future work:

Container Types. In this paper, we attach the smartphone to the wall of a 3D-printed container to measure the viscosity. However, the shape and cell phone placement position may be inapplicable for the current mathematical model. Correspondingly, Therefore, it is necessary to create more complex models that combine not only the diversity of the container, but also the built-in structure of the phone. Furthermore, in practical usage (e.g., restaurant), the user would like to test the liquids in different containers without attaching the smartphone to the sidewall. So, we need to create a more complex model to further deal with these challenging problems.

Temperature. According to the viscosity theory, the higher the temperature, the lower the liquid viscosity. For example, the viscosity of water at 20°C is 1 cP, and it will drop to 0.8 cP at 30°C. Therefore, we need to design a novel calibration scheme based on the relationship between temperature and viscosity.

Complex Component Analysis. If the liquid contains only one molecular component, it can be easily distinguished by viscosity. When the liquid composition is too complex, the interaction force between various molecules is difficult to predict with only a viscosity model. In the future, we will combine with other liquid properties (e.g., density, surface tension, and permittivity) to improve the liquid testing ability on smartphones.

REFERENCES

[1] J. Wang, J. Xiong, X. Chen, H. Jiang, R. K. Balan, and D. Fang, "TagScan: Simultaneous target imaging and material identification with commodity RFID devices," in *Proc. Annu. Int. Conf. Mobile Comput. Netw.*, 2017, pp. 288–300.

[2] U. Ha, Y. Ma, Z. Zhong, T. M. Hsu, and F. Adib, "Learning food quality and safety from wireless stickers," in *Proc. ACM Workshop Hot Topics Netw.*, 2018, pp. 106–112.

[3] Q. Huang, Z. Yang, and Q. Zhang, "Smart-U: Smart utensils know what you eat," in *Proc. IEEE Conf. Comput. Commun.*, 2018, pp. 1439–1447.

[4] A. Dhekne, M. Gowda, Y. Zhao, H. Hassanieh, and R. R. Choudhury, "LiquID: A wireless liquid identifier," in *Proc. 16th ACM Int. Conf. Mobile Syst. Appl. Serv.*, 2018, pp. 442–454.

[5] T. Rahman, A. T. Adams, P. Schein, A. Jain, D. Erickson, and T. Choudhury, "Nutrilyzer: A mobile system for characterizing liquid food with photoacoustic effect," in *Proc. 14th ACM Conf. Embedded Netw. Sensor Syst.*, 2016, pp. 123–136.

[6] S. Yue and D. Katabi, "Liquid testing with your smartphone," in *Proc. 17th Annu. Int. Conf. Mobile Syst. Appl. Serv.*, 2019, pp. 275–286.

[7] C. Tripolino, C. Irace, C. Carallo, F. B. Scavelli, and A. Gnasso, "Body fat and blood rheology: Evaluation of the association between different adiposity indices and blood viscosity," *Clin. Hemorheol. Microcirculation*, vol. 65, no. 3, pp. 241–248, 2017.

[8] J. de Vicente, M. T. López-López, J. D. Durán, and F. Gonz ález-Caballero, "Shear flow behavior of confined magnetorheological fluids at low magnetic field strengths," *Rheologica Acta*, vol. 44, no. 1, pp. 94–103, 2004.

[9] C. Blom and J. Mellema, "Torsion pendula with electromagnetic drive and detection system for measuring the complex shear modulus of liquids in the frequency range 80–2500 Hz," *Rheologica Acta*, vol. 23, no. 1, pp. 98–105, 1984.

[10] W. Y. Shih, X. Li, H. Gu, W. H. Shih, and I. A. Aksay, "Simultaneous liquid viscosity and density determination with piezoelectric unimorph cantilevers," *J. Appl. Phys.*, vol. 89, no. 2, pp. 1497–1505, 2001.

[11] C. Riesch, E. K. Reichel, F. Keplinger, and B. Jakoby, "Characterizing vibrating cantilevers for liquid viscosity and density sensing," *J. Sensors*, vol. 2008, pp. 1–9, 2008.

[12] M. Gottlieb, "Zero-shear-rate viscosity measurements for polymer solutions by falling ball viscometry," *J. Non-Newtonian Fluid Mechanics*, vol. 6, no. 2, pp. 97–109, 1979.

[13] M. Fr öhlich *et al.*, "Association between C-reactive protein and features of the metabolic syndrome: A population-based study," *Diabetes Care*, vol. 23, no. 12, pp. 1835–1839, 2000.

[14] M. R. Weir, "Microalbuminuria and cardiovascular disease," *Clin. J. Amer. Soc. Nephrol.*, vol. 2, no. 3, pp. 581–590, 2007.

[15] H. Eyring, "The activated complex in chemical reactions," *Source Book Chem., 1900–1950*, vol. 3, no. 2, pp. 107–115, 2014.

[16] V. C. A. Ferraro, S. Chapman, and T. G. Cowling, *The Mathematical Theory of Non-Uniform Gases. An Account of the Kinetic Theory of Viscosity, Thermal Conduction, and Diffusion in Gases*, vol. 38. Cambridge, U.K.: Cambridge Univ. Press, 1954.

[17] R. A. Bagnold, "Experiments on a gravity-free dispersion of large solid spheres in a Newtonian fluid under shear," *Proc. Roy. Soc. London. A. Math. Physical Sci.*, vol. 225, no. 1160, pp. 49–63, 1954.

[18] A. E. Simone and L. J. Gibson, "Effects of solid distribution on the stiffness and strength of metallic foams," *Acta Materialia*, vol. 46, no. 6, pp. 2139–2150, 1998.

[19] Apple inc.cmmotionactivitymanager, 2020. [Online]. Available: https://developer.apple.com/documentation/coremotion/cmmotionactivitymanager

[20] E. Candes and M. Wakin, "An introduction to compressive sampling," *IEEE Signal Process. Mag.*, vol. 25, no. 2, pp. 21–30, Mar. 2008.

[21] J. A. Tropp and A. C. Gilbert, "Signal recovery from random measurements via orthogonal matching pursuit," *IEEE Trans. Inf. Theory*, vol. 53, no. 12, pp. 4655–4666, Dec. 2007.

[22] N. E. Huang *et al.*, "The empirical mode decomposition and the hilbert spectrum for nonlinear and non-stationary time series analysis," *Proc. Roy. Soc. London. A: Math. Physical Eng. Sci.*, vol. 454, no. 1971, pp. 903–995, 1998.

[23] X. Han and X. Guo, "Cubic hermite interpolation with minimal derivative oscillation," *J. Comput. Appl. Math.*, vol. 331, pp. 82–87, 2018.

[24] S. McKinley and M. Levine, "Cubic spline interpolation," *College Redwoods*, vol. 45, no. 1, pp. 1049–1060, 1998.

[25] S. J. Estéve and M. E. Johnson, "Reduction of sound transmission into a circular cylindrical shell using distributed vibration absorbers and Helmholtz resonators," *The J. Acoustical Soc. America*, vol. 112, no. 6, pp. 2840–2848, 2002.

[26] J. G. de la Rosa, C. Puntonet, and I. Lloret, "An application of the independent component analysis to monitor acoustic emission signals generated by termite activity in wood," *Measurement*, vol. 37, no. 1, pp. 63–76, 2005.

[27] J. Guzma, R. Berešik, and J. Puttera, "Small-sized seismic-acoustic sensor system based on MEMS accelerometer and MEMS microphone," in *Proc. New Trends Signal Process.*, 2018, pp. 1–6.

[28] H. Wu and M. Siegel, "Correlation of accelerometer and microphone data in the "coin tap test"," *IEEE Trans. Instrum. Meas.*, vol. 49, no. 3, pp. 493–497, Jun. 2000.

[29] A. Ross and G. Ostiguy, "Propagation of the initial transient noise from an impacted plate," *J. Sound Vibration*, vol. 301, no. 1/2, pp. 28–42, 2007.

[30] S. M. Yoon, J. H. Kim, and J. H. Kim, "Mathematical modeling and analysis of vibration characteristics of smart-phone," *Appl. Mechanics Materials*, vol. 284, pp. 800–805, 2013.

[31] C. Feng *et al.*, "WiMi: Target material identification with commodity Wi-Fi devices," in *Proc. IEEE 39th Int. Conf. Distrib. Comput. Syst.*, 2019, pp. 700–710.
[32] Y. Huang, K. Chen, Y. Huang, L. Wang, and W. Kaishun, "Vi-Liquid: Unknown liquid identification with your smartphone vibration," in *Proc. 27th Annu. Int. Conf. Mobile Comput. Netw.*, 2021, pp. 174–187.
[33] S. A. Anand and N. Saxena, "Speechless: Analyzing the threat to speech privacy from smartphone motion sensors," in *Proc. IEEE Symp. Security Privacy*, 2018, pp. 1000–1017.
[34] B. Xie *et al.*, "Tagtag: Material sensing with commodity RFID," in *Proc. 17th Conf. Embedded Netw. Sensor Syst.*, 2019, pp. 338–350. [Online]. Available: https://doi.org/10.1145/3356250.3360027
[35] H. Matsui, T. Hashizume, and K. Yatani, "Al-light: An alcohol-sensing smart ice cube," *Proc. ACM Interactive Mobile Wearable Ubiquitous Technol.*, vol. 2, pp. 1–20, Sep. 2018.
[36] Q. Dai, Y. Huang, L. Wang, R. Ruby, and K. Wu, "mm-Humidity: Fine-grained humidity sensing with millimeter wave signals," in *Proc. IEEE 24th Int. Conf. Parallel Distrib. Syst.*, 2018, pp. 204–211.
[37] Y. Huang, K. Chen, L. Wang, Y. Dong, Q. Huang, and K. Wu, "Lili: Liquor quality monitoring based on light signals," in *Proc. 27th Annu. Int. Conf. Mobile Comput. Netw.*, 2021, pp. 1–13.
[38] I. N. Aribudiman, "Seepage in soil from the difference of water viscosity using Geo-studio SEEP/W program," *Int. Res. J. Eng. IT Sci. Res.*, vol. 5, no. 1, pp. 15–26, 2019.
[39] J. Ma *et al.*, "Liquid viscosity measurement using a vibrating flexure hinged structure and a fiber-optic sensor," *IEEE Sensors J.*, vol. 16, no. 13, pp. 5249–5258, Jul. 2016.
[40] D. Beyssen, L. Le Brizoual, O. Elmazria, and P. Alnot, "Microfluidic device based on surface acoustic wave," *Sens. Actuators B*, vol. 118, pp. 380–385, Oct. 2006.
[41] D. Barron, "Propagation loss measuring device," U.S. Patent 3,810,079, May 7, 1974.
[42] M. Motosuke, J. Shimakawa, D. Akutsu, and S. Honami, "Noncontact manipulation of microflow by photothermal control of viscous force," *Int. J. Heat Fluid Flow*, vol. 31, no. 6, pp. 1005–1011, 2010.
[43] J. Xu, X. Ren, W. Gong, R. Dai, and D. Liu, "Measurement of the bulk viscosity of liquid by brillouin scattering," *Appl. Opt.*, vol. 42, no. 33, 2003, Art. no. 6704.
[44] J. Liu, Y. Chen, M. Gruteser, and Y. Wang, "VibSense: Sensing touches on ubiquitous surfaces through vibration," in *Proc. 14th Annu. IEEE Int. Conf. Sens. Commun. Netw.*, 2017, pp. 1–9.
[45] Y. Huang, S. Cai, L. Wang, and K. Wu, "Oinput: A bone-conductive QWERTY keyboard recognition for wearable device," in *Proc. Int. Conf. Parallel Distrib. Syst.*, 2019, pp. 946–953.
[46] Y. Huang, W. Chen, H. Chen, L. Wang, and K. Wu, "G-Fall: Device-free and training-free fall detection with geophones," in *Proc. 16th Annu. IEEE Int. Conf. Sens. Commun. Netw.*, 2019, pp. 1–9.
[47] Z. Jia *et al.*, "Monitoring a person's heart rate and respiratory rate on a shared bed using geophones," in *Proc. 15th ACM Conf. Embedded Netw. Sensor Syst.*, 2017, Art. no. 6. [Online]. Available: https://doi.org/10.1145/3131672.3131679
[48] S. Pan *et al.*, "FootprintID: Indoor pedestrian identification through ambient structural vibration sensing," *Proc. ACM Interactive Mobile Wearable Ubiquitous Technol.*, vol. 1, pp. 1–31, Sep. 2017.
[49] X. Xu *et al.*, "TouchPass: Towards behavior-irrelevant on-touch user authentication on smartphones leveraging vibrations," in *Proc. 26th Annu. Int. Conf. Mobile Comput. Netw.*, 2020, Art. no. 24. [Online]. Available: https://doi.org/10.1145/3372224.3380901
[50] L. Yang, W. Wang, and Q. Zhang, "VibID: User identification through bio-vibrometry," in *Proc. 15th ACM/IEEE Int. Conf. Inf. Process. Sensor Netw.*, 2016, pp. 1–12.
[51] G. Laput, R. Xiao, and C. Harrison, "ViBand: High-fidelity bio-acoustic sensing using commodity smartwatch accelerometers," in *Proc. 29th Annu. Symp. User Interface Softw. Technol.*, 2016, pp. 321–333. [Online]. Available: https://doi.org/10.1145/2984511.2984582
[52] H. Wen, J. Ramos Rojas, and A. K. Dey, "Serendipity: Finger gesture recognition using an off-the-shelf smartwatch," in *Proc. CHI Conf. Hum. Factors Comput. Syst.*, 2016, pp. 3847–3851. [Online]. Available: https://doi.org/10.1145/2858036.2858466
[53] N. Roy and R. R. Choudhury, "Ripple II: Faster communication through physical vibration," in *Proc. 13th USENIX Conf. Netw. Syst. Des. Implementation*, 2016, pp. 671–684.

Yongzhi Huang (Student Member, IEEE) received the master's degree in college of computer science and software engineering from Shenzhen University, China, in 2020. His research interests include smart sensing, mobile computing and Internet of Things(IoT). He published papers in primer conferences, such as ACM Mobicom, etc. He is the inventor of 12 Chinese pending patents (2 are issued).

Kaixin Chen is currently working toward the 4th-year undergraduate degree in the College of Electronic and Information Engineering, Shenzhen University, China. His research interest include mobile computing and Internet of Things (IoT).

Yandao Huang is currently working toward the graduate degree in the College of Computer Science and Software Engineering, Shenzhen University, China. His research interest include mobile computing, intelligent sensing, and human-computer interaction (HCI).

Lu Wang (Senior Member, IEEE) is currently an assistant professor in the College of Computer Science and Software Engineering, Shenzhen University, China. Her research interests include wireless communications and mobile computing.

Kaishun Wu (Senior Member, IEEE) received the PhD degree in computer science and engineering from the Hong Kong University of Science and Technology, Hong Kong, in 2011. After that, he worked as a research assistant professor at the Hong Kong University of Science and Technology, Hong Kong. In 2013, he joined SZU as a distinguished professor. He has coauthored 2 books and published more than 100 high quality research papers in international leading journals and primer conferences, like the *IEEE Transactions on Mobile Computing*, the *IEEE Transactions on Parallel and Distributed Systems*, ACM MobiCom, IEEE INFOCOM. He is the inventor of 6 U.S. and more than 90 Chinese pending patents. He received 2012 Hong Kong Young Scientist Award, 2014 Hong Kong ICT awards: Best Innovation and 2014 IEEE ComSoc Asia-Pacific Outstanding Young Researcher Award. He is an IET fellow.